**Title**
NUCLEON AND NUCLEAR CROSS SECTIONS FOR POSITIVE PIONS AND PROTONS ABOVE 1.4 BeV/c



**Author**
Longo, Michael J.

**Publication Date**
1961-02-01

Ja

UCRL 9497

UNIVERSITY OF
CALIFORNIA

*Ernest O. Lawrence*

# *Radiation Laboratory*

## NUCLEON AND NUCLEAR CROSS SECTIONS FOR POSITIVE PIONS AND PROTONS ABOVE 1.4 Bev/c

## DISCLAIMER

UCRL-9497
UC-34 Physics
TID-4500 (16th Ed.)

UNIVERSITY OF CALIFORNIA
Lawrence Radiation Laboratory
Berkeley, California

Contract No. W-7405-eng-48

# NUCLEON AND NUCLEAR CROSS SECTIONS FOR POSITIVE PIONS AND PROTONS ABOVE 1.4 Bev/c

Michael J. Longo

(Thesis)

February 1961

Contents

# NUCLEON AND NUCLEAR CROSS SECTIONS FOR POSITIVE PIONS AND PROTONS ABOVE 1.4 Bev/c

Michael J. Longo

Lawrence Radiation Laboratory
University of California
Berkeley, California

February 1961

## ABSTRACT

1. Total $(\pi^+, p)$ and $(p, p)$ cross sections in the momentum range 1.4 to 4.0 Bev/c are presented. These measurements, with an accuracy of $\approx 2\%$, were made at the Berkeley Bevatron using counter techniques. Pions were distinguished from protons by means of a gas-filled Cerenkov counter. The $(\pi^+, p)$ total cross section was found to be almost constant above 2.0 Bev/c at a value near 29 mb. The $(p, p)$ cross section decreases gradually from 47.5 mb to 41.7 mb over the momentum range covered.

2. Transmission measurements of $\pi^+$-nucleus and p-nucleus cross sections in both good and poor geometry were made at 3.0 Bev/c. The results are compared with the predictions of the optical model and dispersion relations. In contrast to most previous work at high energies, an essentially exact solution of the wave equation for a potential well with a diffuse edge was used. The values of the imaginary part of the optical potential that best fit the experimental data are in good agreement with the predicted values. No strong conclusions regarding the real part of the potential are possible. Absorption and total elastic cross sections for Be, C, Al, and Cu are presented. The total elastic cross sections from this experiment disagree with Wikner's for $\pi^-$-nucleus scattering.

## I. INTRODUCTION

One of the most promising developments in the study of the interaction of mesons and nucleons has been the application of dispersion relations. To date the most useful result has been to provide a means for calculating the real part of the pion-nucleon forward scattering amplitude. According to dispersion relations, the real part of the forward scattering amplitude in the laboratory system is given by

$$\mathrm{Re}\left[f_{\pm}(k)\right] = 1/2(1 \pm \omega/m) \cdot \mathrm{Re}\left[f_{+}(k=0)\right] + 1/2(1 \mp \omega/m) \cdot \mathrm{Re}\left[f_{-}(k=0)\right] + \frac{k^2}{4\pi^2} \int_m^\infty \frac{d\omega'}{k'} \frac{\sigma_{\pm}(\omega')}{\omega'-\omega} + \frac{k^2}{4\pi^2} \cdot \int_m^\infty \frac{d\omega'}{k'} \frac{\sigma_{\mp}(\omega')}{\omega'+\omega} \pm \frac{2f^2}{m^2} \frac{k^2}{\omega \mp m^2/2M}, \tag{1}$$

where $k$ and $\omega$ are, respectively, the pion wave number and total energy in the laboratory system, $m$ is the pion mass, $M$ the nucleon mass, $f^2$ the pion-nucleon coupling constant, and $\sigma_{\pm}(\omega')$ the total $(\pi^{\pm}\text{-p})$ cross section at energy $\omega'$.[1] The units in Eq. (1) are such that $\hbar = c \equiv 1$, and the principal values of the integrals are to be taken.

There have been many important applications of dispersion relations to pion-nucleon interactions at energies below 0.5 Bev. In order to extend their usefulness to energies on the order of 1 Bev, it is necessary to know the total cross section at considerably higher energies. Measurements have been made to about 1.8 Bev, but little accurate data are available above this energy, especially for $\pi^+$ scattering. One of the purposes of this paper is to report the results of a measurement of the total $\pi^+$-p cross section in the momenta range 1.4 to 4.0 Bev/c. In addition, p-p total cross sections were measured simultaneously in the same momentum range.

There is as yet little experimental evidence for the validity of dispersion relations at energies $\gtrsim$ 1.5 Bev. In this region it is possible to make an indirect test by studying the scattering of pions on nuclei.

The optical model of the nucleus leads to a relation between the average potential seen by a pion traversing the nucleus and the forward scattering amplitude for pion-nucleon scattering. If this potential can be determined experimentally with sufficient accuracy, it is in principle possible to test the predictions of the optical model and dispersion relations simultaneously. The uncertainty in the predicted optical-model potential is approx 10% because of second-order effects which are not very well known.

It was possible in this experiment to measure cross sections for several nuclei with the same equipment used to measure the total $\pi^+$-p and p-p cross sections. This was done at 3.0 Bev/c for Be, C, Al, and Cu with various geometries. The results are used to determine best-fit optical potentials, which are compared with the predicted values.

The experimental techniques used are discussed in Sections II and III of this paper. The measured cross sections are presented in Section IV. In Section V the analysis of the nuclear cross sections in terms of the optical model is given, and "best-fit" values for the parameters describing the nuclear potential are discussed. In contrast to most previous attempts to make fits of this type to high-energy scattering data, those presented here were made by using an essentially exact solution of the wave equation for a complex potential well with a diffuse edge. This was possible through the use of a high-speed electronic computer (the IBM 704). Section VI discusses the implications of these results.

## II. EXPERIMENTAL METHOD AND EQUIPMENT

### A. General Description of Method

In these measurements, made at the Berkeley Bevatron, a beam consisting primarily of a mixture of positive pions and protons of well-defined momentum was collimated by means of a counter telescope. Pions were separated from protons electronically by using a gas-filled Cerenkov counter. This allowed simultaneous measurements of pion and proton cross sections. The basic arrangement is shown in Fig. 1.

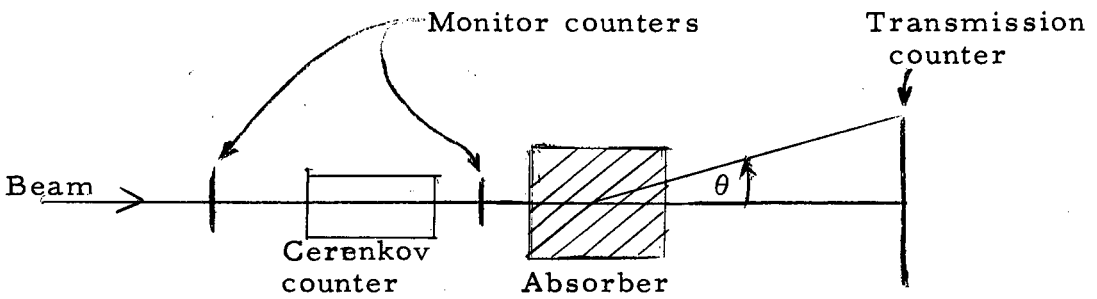


Fig. 1. Arrangement of apparatus.

After passing through the monitor telescope, the beam is allowed to strike an absorber. The fraction of the beam scattered through an angle greater than $\theta$ or removed by inelastic processes is determined by means of another counter placed after the absorber. If the angle $\theta$ is such that most of the particles scattered in nuclear interactions miss this transmission counter, we have the situation traditionally referred to as a "good-geometry" measurement.

If the angle $\theta$ is increased, more and more of the elastically scattered particles strike the transmission counter, and the apparent

cross section decreases. In the idealized experiment we are discussing, the apparent cross section $\sigma(\theta)$ is given by

$$\sigma(\theta) = -\frac{1}{nx} \log N/N_0, \qquad (2)$$

where $N/N_0$ is the fraction of the beam transmitted for a particular value of $\theta$, and $nx$ is the number of nuclei per $cm^2$ as seen by the incoming beam. The expected variation of $\sigma(\theta)$ with the solid angle subtended by the transmission counter is depicted in Fig. 2 (see also Figs. 20 and 21). At very small angles the curve rises sharply because

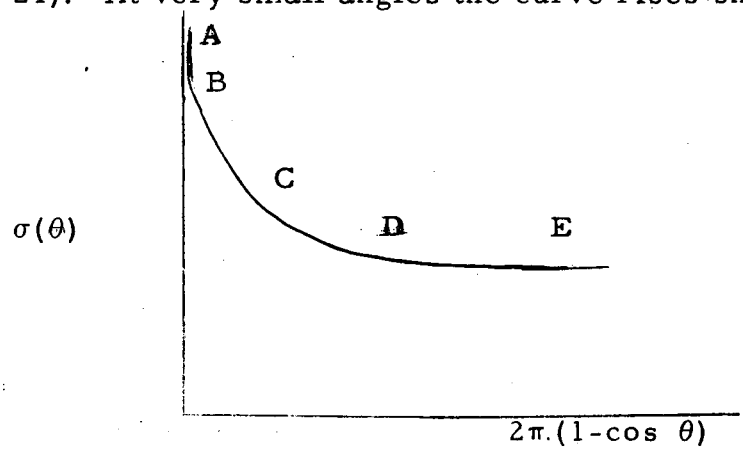


Fig. 2. Variation of cross section with subtended angle.

of Rutherford scattering (the portion AB of the curve). As $\theta$ is increased, a point is reached where most of the Rutherford scattering is contained, but the majority of particles undergoing nuclear interactions are scattered out of the cone subtended by the detector (Point B). It is instructive to note here that the slope of such a plot of $\sigma(\theta)$ vs solid angle in the region BCD is $(d\sigma/d\Omega)_{el}$, the differential elastic cross

section.* At high energies the elastic scattering is strongly peaked forward, with an angular distribution characteristic of diffraction scattering. Most of the elastic scattering is therefore confined to angles $\lesssim (kR)^{-1}$, where k is the wave number of the incident particle and R is the radius of the nucleus. Thus for $\theta \gg (kR)^{-1}$, the curve for $\sigma(\theta)$ is almost flat and is approximately equal to the inelastic cross section (the region DE in Fig. 2).

In this experiment measurements of $\sigma(\theta)$ were made over this entire range of angles for beryllium, carbon, aluminum, and copper absorbers, with 3.0-Bev/c pions and protons. For hydrogen, measurements were made only in the region BC in Fig. 2 because of the large angles involved. This part of the curve can be extrapolated to $\theta = 0$ to give the total nuclear cross section.

The techniques used for the hydrogen and heavy-nuclei measurements were basically the same. Each measurement consisted of a cycle of runs with target full (or target in) preceded and followed by target-empty runs. A complete cycle generally lasted about 4 hours. The sequence of runs was usually two runs with target empty, four runs with target full, followed by two more runs with target empty. Successive runs were compared for reproducibility as a check on equipment operation. Frequent checks were also made with a test pulser.

## B. Beam Geometry

The over-all experimental arrangement is shown in Fig. 3. It is unusual in that the apparatus was set up on the inside of the Bevatron ring. This was done in order to obtain a positive pion beam of as high a momentum as possible. The production of high-energy particles at the Bevatron target is strongly peaked forward so that it is necessary to take

*There is also a contribution to the slope due to charged secondary particles which are produced in inelastic collisions. As $\theta$ is increased more of these strike the detector, and the apparent cross section decreases.

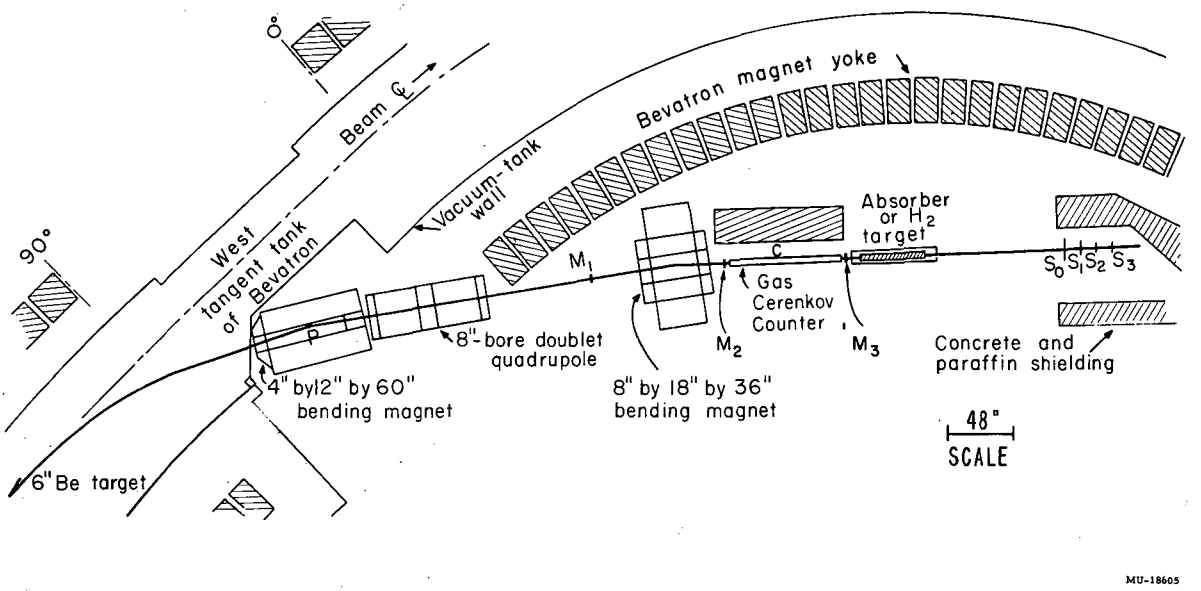


Fig. 3. Experimental arrangement. Magnetic shielding has been omitted for clarity.

a high-energy beam off at a small angle from the circulating proton beam. The positive particles are then bent inward toward the center of the Bevatron by the magnetic field.*

In the course of the experiment three different Bevatron targets were used. Each target consisted of 6 inches of beryllium with a 0.125-inch-thick polyethylene lip. The same targets were also used by another experimental group that ran simultaneously and had control of Bevatron operation. Wherever possible our experiment was designed so that any of the targets could be used interchangeably.

The proton beam was allowed to spill onto the target for a period of 150 milliseconds by passing a "foil" consisting of several strands of nylon thread through the beam. This caused the proton beam to spiral in and strike the beryllium target. In the process of spiralling in, the beam loses most of its rf structure so that a more favorable duty cycle is obtained.

A 12-in. by 60-in. bending magnet was used to bend the emerging pion beam farther from the Bevatron structure. This gave a smaller takeoff angle at high momenta and provided a means for deflecting pions of different momenta into the beam line. The takeoff angles ranged from about + 9 deg at 1.4 Bev/c to -15 deg at 4.0 Bev/c (positive angles measured outward away from the center of the Bevatron). The orbits of the particles in the Bevatron were determined by using a computer program for the IBM 650 together with measured magnetic field profiles. This program traces out the orbits of the particles, given their momentum and angle of emergence from the target. At each momentum, rays that connect the target and point P in Fig. 3 were found, essentially by a process of trial and error. The currents required

---

*If the target were put in a straight section of the Bevatron, a takeoff angle of approx 25 deg would be required to clear the Bevatron structure. Kinematically, the maximum energy a pion produced at this angle can have is 3.3 Bev; useful fluxes cannot be obtained at energies much greater than 2.5 Bev.

in the bending magnet to deflect these "rays" through the proper angles were then determined by wire-orbit measurements.

Estimating the error involved in the momentum determination is difficult. Some of the possible sources of error are:

1. The uncertainty in the Bevatron's magnetic field and in the method of determining orbits. - The Bevatron's magnetic field near the beam center line is known to about ±1/2 %. The measurements of the field near the edges of the pole were accurate to about ±2 %. The field values used were for a time in the Bevatron cycle near the center of the beam spill. The change in magnetic field over the spill time caused a deviation of approximately ±1.5% about the nominal momentum. Most of the orbits calculated by the IBM 650 computer were checked with an analogue computer known as "the Bug," which traces the orbits on a contour plot of the magnetic field. Both methods agreed within 1%.

2. The uncertainty in the field of the 12-by-60-in. magnet. - The wire-orbit measurements on this magnet had an accuracy of about 1%.

3. The uncertainty in positioning of targets, magnets, and counters. - The positions of the counters and magnets were surveyed with an accuracy on the order of ±1/8 in. The positions of the Bevatron magnet pole tips and the target positions are also known to about this accuracy.

4. Stray magnetic fields due to the proximity of the beam line to the Bevatron. - Without shielding, the stray magnetic field along the beam line varied from a few gauss to a few hundred gauss, depending on the proximity to the Bevatron magnet. Extensive magnetic shielding (not shown in Fig. 3) was employed to reduce this to a negligible value.

5. Energy loss in the counters and other material in the beam. - This was only about 70 Mev, and the assigned momenta were corrected to take this loss into account.

It is difficult to estimate the over-all uncertainty in momentum due to these factors. A reasonable value is thought to be ±2 %. The momentum spread in the beam is estimated at ±2.5% due, in large part,

to the change in the Bevatron's magnetic field during the time the proton beam was being spilled onto the target.

Immediately following the 12-by-60-in. bending magnet was an 8-in.-bore quadrupole whose main function was to increase the solid angle accepted by the counter telescope. Operating currents for this quadrupole were determined by wire orbits. In order to decrease Coulomb scattering corrections to the cross-section measurements, an attempt was made to produce an image of the Bevatron target near the transmission counters $S_1$, $S_2$, $S_3$. (See Section III. C for further discussion.) However, because of the scattering of the beam in the monitor counters (especially the gas Cerenkov counter), only a very poor image was produced at the lower momenta. Since the focusing was not at all critical, no beam time was used to tune the quadrupole. A 3-in.-thick iron shield was placed around the quadrupole to reduce the Bevatron's magnetic field to a low value.

A second bending magnet with an 18-by-36-in. pole tip followed the quadrupole (see Fig. 3). The purpose of this magnet was to bend the beam away from the Bevatron, making the magnetic shielding problem much simpler and allowing somewhat more space for the apparatus. Because the magnet was so close to the Bevatron, its field tended to pulse with that of the Bevatron. Measurements of the time-varying component of the field in the magnet gap were made with a search coil. In the worst case this amounted to 1.5% of the steady field. Because it was so close to the telescope counters, this magnet had very little effect on the momentum selection, and this variation was not considered significant.

## C. The Counter System

The monitor telescope consisted of scintillation counters $M_1$, $M_2$, and $M_3$ and a gas Cerenkov counter C. All scintillators consisted of machined discs of polystyrene with 3% terphenyl. Counters $M_1$ and $M_2$ were each 1-1/2 inches in diameter, and $M_3$ was 1 inch in

diameter. The total length of the monitor telescope was 16 feet. The construction and operation of the gas Cerenkov counter have been described elsewhere.[2] In this experiment it was filled with sulfur hexafluoride to a pressure of 10 atmospheres (absolute). This gave a threshold velocity of 0.992 c and allowed a complete separation of pions and protons over the energy range of this experiment. A quadruple coincidence in $M_1$, $M_2$, C, and $M_3$ was required for a pion, and a triple coincidence between $M_1$, $M_2$, and $M_3$ with C in anticoincidence was required for a proton count.

Absorbers were placed in the beam behind $M_3$. The fraction of the beam transmitted was measured at three solid angles simultaneously by scintillation counters $S_1$, $S_2$, and $S_3$. An additional coincidence in $S_0$ was required to keep accidentals to a very low rate. Counter $S_0$ and the transmission counters $S_1$, $S_2$, and $S_3$ consisted of discs of plastic scintillator 1/2 in. thick, viewed edgewise through lucite light pipes by RCA type 6810A phototubes. The phototubes were carefully shielded against stray magnetic fields. These counters ranged in size from 4-1/2 to 12 inches in diameter. Each was tested for uniformity of response over its entire area with a beta source. By suitable treatment of the internal reflecting surfaces of the counters, it was possible to reduce the variations in pulse height to less than ±15% between different parts of the counter. To insure an efficiency near 100%, all counters were operated at voltages such that coincident pulses were about twice as large as required to drive the concidence circuits to saturation.

## D. Electronics

A simplified block diagram of the electronics used is shown in Fig. 4. All components are more or less stock items at the Lawrence Radiation Laboratory. The coincidence circuits were of the type described by Wenzel.[3] With the clipping lines employed, the resolving time was about $6\times10^{-9}$ sec. The standard units have three coincidence channels and one anticoincidence channel. The input pulses can be

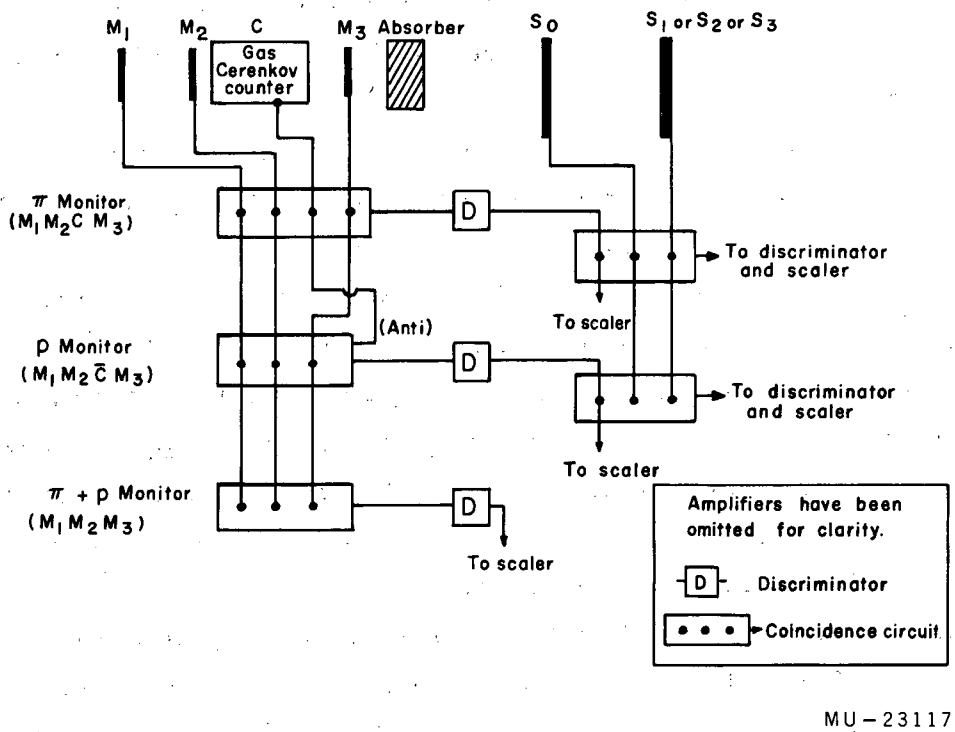


Fig. 4. Simplified block diagram of electronics. For clarity, only one transmission counter is shown.

brought back out of the chassis with very little deterioration of the signal. For this experiment a special unit with four coincidence channels was built for the pion monitor ($M_1M_2C\,M_3$ coincidences). The proton flux was monitored by a standard unit which measured $M_1M_2C\,M_3$ coincidences (the bar denotes an anticoincidence). As a check on the monitors, the number of $M_1M_2M_3$ coincidences was also measured.

The output of the monitor coincidence circuits was used to drive a discriminator-amplifier that provided a shaped pulse used as an input to a second coincidence circuit where a coincidence with $S_0$ and $S_1$ (for example) was required. These discriminators, described in Ref. 4, are capable of handling pulse rates up to $10^7$/sec and are quite stable in operation. The output pulse is satisfactory for driving a Wenzel-type coincidence circuit, providing the clipping lines are not too short. Hewlett-Packard Type 520A prescalers followed by Radiation Laboratory 1000 scalers were employed. These prescalers are capable of counting up to $10^7$ pulses/sec. Our instantaneous counting rates ranged from $10^5$/sec to $10^2$/sec, depending on the beam energy.

Several extra coincidence units and scalers were used to monitor various types of accidentals. Generally, these were quite low. In particular, the accidental rate in the Cerenkov counter never exceeded 2% of the counting rate for pions.

### E. The Hydrogen Target and Other Absorbers Used

The liquid hydrogen target used consisted of a 48-in.-long mylar vessel 4 in. in diameter. Liquid hydrogen was supplied by gravity feed from a large reservoir directly above the target vessel. Both the reservoir and target vessel were surrounded by a heat shield at liquid nitrogen temperature and enclosed in a vacuum. The construction of the target is described in detail in Ref. 5.

The target could be filled and emptied by means of controls located outside the Bevatron shielding wall so that it was not necessary

to shut off the machine for these operations. The level of hydrogen in the reservoir and target vessel was constantly monitored by means of Magnehelic gauges that measured the pressure difference between the bottom and the top of the liquid hydrogen.

The density of liquid hydrogen at its normal boiling point is 0.0 710 g/cm$^3$, from data in Ref. 6. From this should be subtracted the density of hydrogen gas in the empty target. The temperature of the gas was assumed to be that of the liquid, 20.3$^o$ K. The density of hydrogen gas at this temperature is 0.0013 g/cm$^3$. [6]

The other absorbers used were machined blocks of beryllium, graphite, aluminum, and copper, whose purity exceeded 99%. The thicknesses of the absorbers were chosen so that multiple Coulomb scattering corrections would be small for the smallest angles at which measurements were planned. The thicknesses used are listed in Table III (see Sec. IV).

## III. METHOD OF CALCULATING CROSS SECTIONS AND TREATMENT OF DATA

### A. Calculation of Cross Sections

The apparent cross section $\sigma(\theta)$ for a given geometry was calculated from the relation

$$\sigma = (-1/nx) \log (R_F/R_E) \qquad (2a)$$

where $R_F$ and $R_E$ represent the ratio of surviving pions (or protons) to monitor counts with target full and target empty, respectively. Both the number of surviving particles and the monitor counts were corrected for accidentals. As mentioned previously, these corrections were quite small.

### B. Calculation of the Statistical Errors

In general, if there are $M$ monitor counts and $S$ particles surviving, then the standard deviation in $S$ is given by

$$\left\langle (\Delta S)^2 \right\rangle^{1/2} = \sqrt{M} \cdot \sqrt{\bar{R}(1-\bar{R})} , \qquad (3)$$

where $\bar{R}$ is the limiting value of the ratio of $S/M$ when $M$ approaches $\infty$. We can replace $\bar{R}$ by the observed value of $S/M$, and Eq. (3) then becomes

$$\left\langle (\Delta S)^2 \right\rangle^{1/2} = \sqrt{S} \cdot (1 - S/M)^{1/2} . \qquad (3a)$$

For $S/M \ll 1$, Eq. (3a) becomes the usual "square root of the number of counts" formula. In this case, however, $S/M \approx 0.9$, and therefore this approximation is not valid.

C. Corrections for Multiple Coulomb Scattering

When the angle subtended by the transmission counter is made small, the observed cross sections rise sharply owing to the loss of particles by multiple Coulomb scattering in the absorber. Although it is possible to correct for this loss, in practice the corrections are difficult to make and are quite sensitive to the choice of parameters. A general method for applying these corrections to experiments of this type is described by R. M. Sternheimer.[7] He assumes that Coulomb scattering has a Gaussian distribution in angle, with a root-mean-square space angle $\theta_{rms}$ given by

$$\theta_{rms} = (E_s/\beta pc)\sqrt{L/L_{rad}}, \qquad (4)$$

where $E_s = 21$ Mev, $p$ and $\beta c$ are the momentum and velocity, respectively, and $L/L_{rad}$ is the thickness of the absorber in radiation lengths. Sternheimer's paper contains graphs for the fraction of the beam surviving as a function of two parameters related to the geometry and the absorber thickness.

To apply this method it is necessary to have an accurate knowledge of the distribution of beam particles over the surface of the transmission counter at each energy. This was obtained with a 1/4-in.-square scintillation counter in coincidence with the monitor telescope. The counter could be moved vertically or horizontally by means of small motors, and its position could be determined by means of a pair of resistance bridges coupled to the slides that moved the counter. In this way beam profiles could be obtained without shutting off the Bevatron to move the counter. The profile for the 2.97-Bev/c beam used for the heavy-nuclei measurements is shown in Fig. 5. At lower energies the profiles were broader, primarily as a result of multiple Coulomb scattering in the Cerenkov counter.

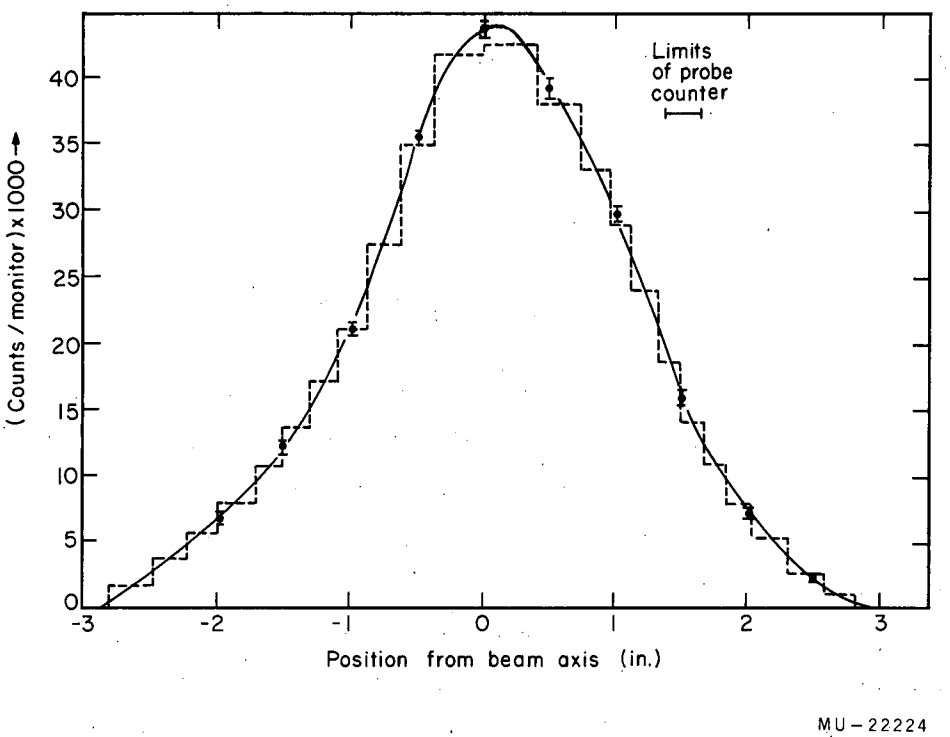


Fig. 5. Horizontal beam profile at 3.0 Bev/c. The vertical profile is quite similar.

When Sternheimer's method was applied, the actual distribution was approximated by a sum of rectangular distributions (the dotted line in Fig. 5). The fraction lost for each part was calculated, and the contributions summed.

In attempting to correct the experimental points most affected by Coulomb scattering it was found that if $\theta_{rms}$ from Eq. (4) was used the corrections were too large — the corrected values of $\sigma(\theta)$ fell well below the trend established by the points at large $\theta$ where no corrections were necessary. In view of the approximations involved in the derivation of Eq. (4) this result is not surprising.* It was found that the value of $\theta_{rms}$ from Eq. (4) had to be reduced by 30% to obtain good over-all agreement.

Even with this modification, the results were not always completely satisfactory, so that the Coulomb corrections were assigned an error of ±25% or more, depending on the knowledge of the beam profile. These corrections were important only in the low-energy hydrogen data when the solid angle subtended by the transmission counter was small. It was found that no corrections were necessary to the heavy-element data at any angles at which measurements were made. Furthermore the effect of the large error assigned to the Coulomb scattering corrections to the hydrogen data was to minimize the statistical weight of the small-angle points so that they had little effect on the extrapolated total cross section. (See next section.)

### D. The Extrapolation of the Hydrogen Data to Obtain the Total Cross Section

In the case of hydrogen only the total cross sections for nuclear scattering were to be measured. In order to obtain an accurate value it is desirable to have the solid angle subtended by the transmission

*On the basis of a more theory, Barkas and Rosenfeld suggest that the value of $\theta_{rms}$ given by Eq. (4) be reduced by 20% (Ref. 8).

counter as small as possible so that nearly all the particles undergoing nuclear scattering are removed from the beam. An effective lower limit is set by multiple Coulomb scattering at small angles, however; thus in practice a small correction must be applied to the measured cross sections because of the nonzero solid angle subtended by the counter. This was done by taking measurements at several solid angles and extrapolating the measured cross sections to zero solid angle. A linear dependence on solid angle was assumed. From the discussion of Sec. III. A, the slope of the extrapolation is $(d\sigma/d\Omega)_{el}$ plus a contribution due to the detection of charged secondaries. Neither of these terms is expected to vary significantly over the range of angles involved (0 to 2 deg).

Data were taken at six solid angles ranging from $0.6\times10^{-3}$ to $4.2\times10^{-3}$ steradian as measured from the center of the hydrogen. After corrections for multiple Coulomb scattering were made, no significant deviation from the expected linear dependence on solid angle was observed. The extrapolation increased the cross sections at intermediate solid angles by about 2%.

## E. Contamination in the Beam

### 1. Contamination in the Pion Beam

The gas Cerenkov counter provided a very useful means for determining the muon and electron contamination in the beam. If the gas pressure in the counter is raised gradually from a low value, first the electrons begin to count, then the muons, and later the pions. In this case, because of the small difference in velocities, it was possible to separate the muons and pions only at the lower energies. Figure 6 shows the ratio of $M_1M_2\bar{C}M_3$ coincidences to $M_1M_2M_3$ coincidences plotted against the index of refraction of the gas in the counter, for a beam momentum of 1.8 Bev/c. The threshold for 1.8-Bev/c muons and pions is also indicated. It is apparent that the muon contamination is small, probably less than 1% of the number of pions. The tail on the curve at low indices of refraction is presumably due to electrons.

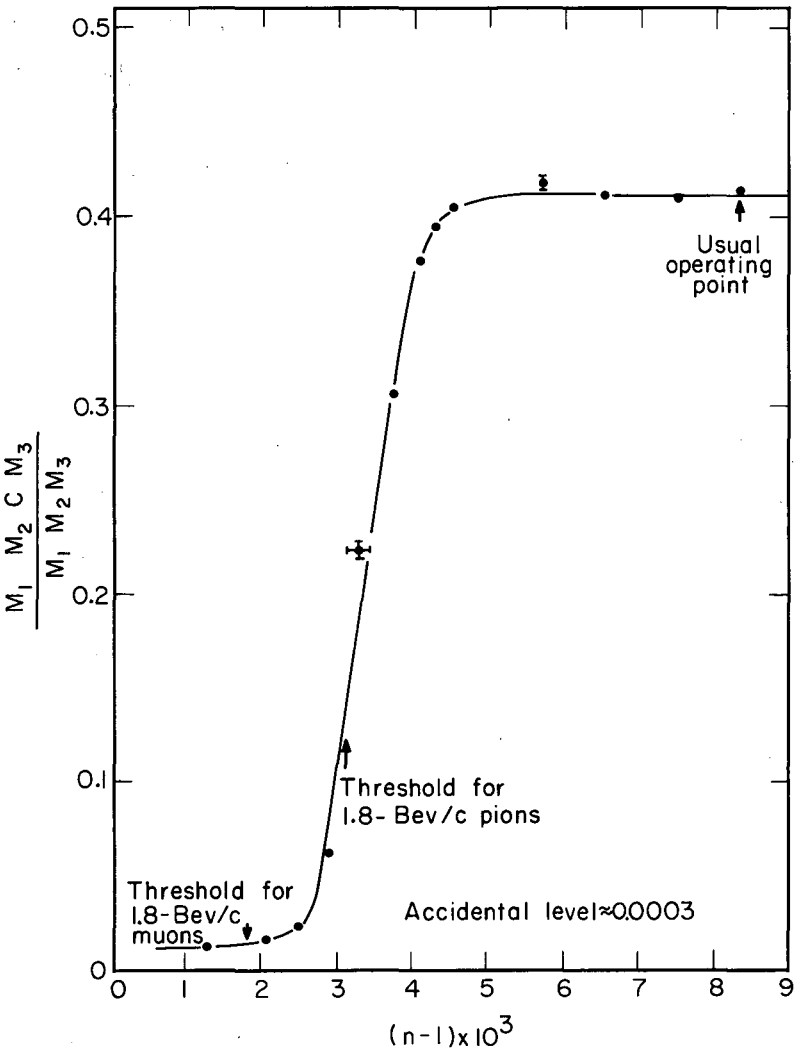


Fig. 6. Cerenkov counter index-of-refraction curve at 1.8 Bev/c.

a. Calculation of the muon contamination. A curve such as in Fig. 6 indicates only the fraction of muons that are formed before the last bending magnet and thus have approximately the same momentum as the pions. Muons that are formed after the last bending magnet have a large spread in momentum and so do not cause a sharp rise in the index-of-refraction curve. For this reason the total muon contamination in the beam at each energy was determined by calculation. To do this, the beam line was broken up into segments. The probability of a pion's decaying between points $X_1$ and $X_2$ is given by

$$N(X_1) - N(X_2) = N_0 [\exp(-X_1/\lambda) - \exp(-X_2/\lambda)], \qquad (5)$$

where $\lambda = \beta \gamma c \tau_0$ is the mean life in centimeters. It was then necessary to determine the probability for the muon to come off in such a direction that it would pass through the counter system. The contributions of all segments were then summed to get the fraction of muons in the beam.

Because of the complication caused by the Bevatron's magnetic field and the quadrupole, it was possible to calculate the contribution from the region before the last bending magnet only approximately. However, it was found that the total yield from this region was less than 0.2%. This is supported by the Cerenkov counter curve, which also indicates it is very small.

The calculation for the region following the last bending magnet was much simpler. Because there is no momentum selection, it is necessary only to calculate the solid angle subtended by the "limiting aperture" of the system (either $M_3$ or the transmission counter).*

*Note that in general the muon contamination depends on the solid angle subtended by the transmission counter. The corrections for muon contamination were therefore different for each counter.

This solid angle is then transformed into the center-of-mass system of the decaying pion. Since the decay is isotropic in this system, the probability of the muons passing through the counters is just $1/4\pi$ times this solid angle. The only important simplification in these calculations was that the finite diameter of the beam was neglected. The maximum correction in the pion cross sections was 2%, which justifies such a simplification.

b. Calculation of the Electron Contamination. Another contaminant in the pion beam at low energies was electrons. From Fig. 6 we can estimate their number at about 3% of the number of pions at 1.8 Bev/c, the energy at which the Cerenkov counter pressure curve was taken.* No measurements were made at other momenta because of limitations on running time.

The major source of these electrons is the decay of $\pi^0$ mesons produced in the Bevatron target. These mesons decay almost immediately into two gamma rays, either of which can in turn produce an electron pair in the target material. The probability of producing a pair is roughly proportional to the available path length L in the target material (Fig. 7).

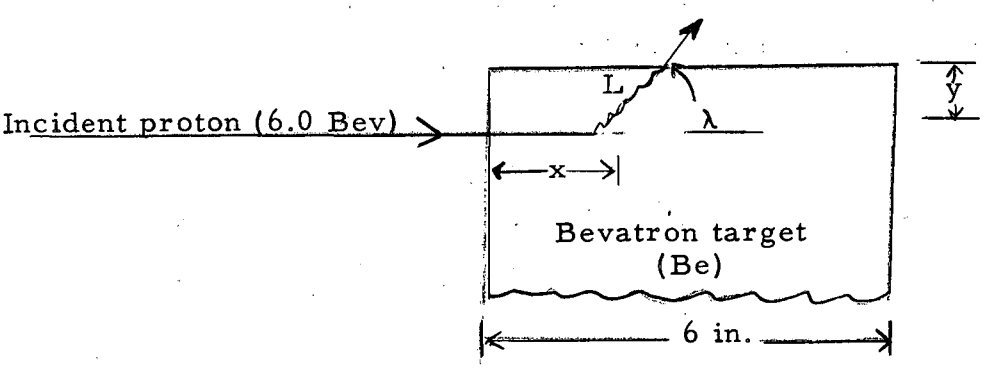


Fig. 7. Geometry for electron production in Bevatron target.

*Because most of the actual data near this energy were taken with a different Bevatron target, this result does not necessarily apply to neighboring energies.

It was possible to calculate the electron contamination $e^+/(e^+ + \pi^+)$ in the beam at each momentum by using theoretical estimates of the yield of pions produced in the Bevatron target.[9] The calculation is described in detail in Appendix I. Briefly, the theoretical curves for $\pi^0$ production were used to estimate the spectrum of high-energy gamma rays. This was in turn used to calculate the electron yield from pair production relative to that of positive pions. The average path length $\bar{L}(\lambda)$ was calculated by using theoretical curves for the distribution in $y$ of the proton flux striking the target. (See Fig. 7.)

For the conditions under which the Cerenkov counter curve (Fig. 6) was taken the electron contamination was calculated to be 2.7% of the pion flux, in good agreement with the value of 3% estimated from Fig. 6. Table I lists the calculated values of $e^+/(e^+ + \pi^+)$ for the various beams used in this experiment. An uncertainty of ±50% was assigned to the calculated values. Table I also lists the takeoff angle $\lambda$.

Except for Coulomb scattering, electrons and muons behave as particles with essentially zero cross section. The measured cross sections were first corrected for multiple Coulomb scattering where necessary. The cross section corrected for muon and electron contamination is then given by

$$\sigma^c = \left( \frac{e^+ + \mu^+ + \pi^+}{\pi^+} \right) \sigma . \qquad (6)$$

Table I. Electron contamination

| Momentum (Bev/c) | λ (deg) | % Electrons |
|---|---|---|
| 1.42 | 8.7 | 2.0 ± 1.0 |
| 1.60 | 5.1 | 2.5 ± 1.3 |
| 1.73 | 7.6 | 1.6 ± 0.8 |
| 1.89 | 0.2 | 2.9 ± 1.5 |
| 2.05 | 1.9 | 2.2 ± 1.1 |
| 2.47 | -5.0 | 1.8 ± 0.9 |
| 2.97 | -8.0 | 1.0 ± 0.5 |
| 3.58 | -12.7 | 0.2 ± 0.1 |
| 4.00 | -14.4 | 0 ± 0 |

c. Possible Proton Contamination in the Pion "Beam." It was possible for a proton to be labeled a "pion" if it was associated with a count in the Cerenkov counter. One way this can occur is by an accidental coincidence with an unrelated pulse from the Cerenkov counter. This accidental rate was monitored constantly and corrections were applied to the data. At no time did it exceed 2% of the number of pions. A second possibility is for the proton to count by forming a fast knock-on electron in the Cerenkov counter. The probability of this occurence was estimated to be about 1% at 4.0 Bev/c, which was by far the worst case because of the very high ratio of protons to pions in the beam.

2. Contamination in the Proton Beam

Any beam particle that did not count in the Cerenkov counter was classed as a "proton." This would include $K^+$ mesons and heavier particles. Data of Burrowes et al. at 1.75 Bev/c indicate a yield of approximately six $K^+$ mesons per $10^{10}$ protons incident on their target with a momentum acceptance of ±2% and an estimated solid angle of $0.5\times10^{-3}$ steradian.[10] Comparing this value with the proton yields observed at

1.73 Bev/c in this experiment, one obtains a ratio $>10^3$ protons per $K^+$. This ratio would be expected to be still larger at higher energies.

If the gas Cerenkov counter and the associated anticoincidence circuits were not 100% efficient in removing pions from the protons channels, the result would be an effective pion contamination in the "proton beam." No experimental means of checking this was available, though the flatness of the index-of-refraction curve (Fig. 6) at high indices indicates that this counter is nearly 100% efficient when operated in coincidence. (See also Ref. 2.) The efficiency in anticoincidence was therefore assumed to be $100\%\ ^{+0\%}_{-5\%}$, and the errors in the proton total cross sections increased correspondingly.

### F. A Summary of the Sources of Error Considered in Assigning Errors to the Cross Sections

The following sources of error were taken into account in assigning errors to the total cross sections. All errors were combined in quadrature.

1. The statistical errors in the measurements were considered. These were generally quite small ($\approx 1\%$). The quoted errors also include a fluctuation outside of statistics which was observed in the data. Its magnitude was estimated from the reproducibility of the measured cross sections. At each energy from two to five independent measurements of the cross section were made. (By a "measurement" we mean a sequence of target-empty – target-full runs as described in Sec. II. A. Data were taken at three solid angles simultaneously.) An analysis of the repeated runs showed that the probable error in a single measurement was $\pm 1.4\%$ in addition to the statistical error.

2. At each energy and solid angle all the runs were averaged and the errors combined. The cross sections were then corrected for multiple Coulomb scattering, and the uncertainty in this correction was combined with the other errors.

3. The uncertainty in the extrapolation to zero solid angle was taken to be equal to the uncertainty in slope multiplied by the average

solid angle.

4. The final error in the pion cross sections also includes the uncertainty in the electron contamination in the beam. The errors introduced by the uncertainty in the muon contamination in the pion beam and $K^+$ contamination in the proton beam were considered negligible.

5. The errors in the proton total cross sections also include the uncertainty in the efficiency of the gas Cerenkov counter and the associated electronics, as described in the previous section.

The errors in the heavy-nuclei cross sections include only the statistical errors and the errors due to the random fluctuations outside of statistics, as described above.

# IV. EXPERIMENTAL RESULTS

## A. Total Cross Sections for Positive Pions and Protons on Hydrogen in the Momentum Range 1.4 to 4.0 Bev/c

The measured $\pi^+$-p and p-p total cross sections are listed in Table II and plotted in Fig. 8 as a function of beam momentum. Smooth curves have been drawn to show the gross features of the momentum dependence. The results from other experimenters are also shown for comparison.[11] In general, the agreement is good in regions where an overlap occurs.

Table II. Total $(\pi^+, p)$ and $(p, p)$ cross sections.

| Momentum (Bev/c) | $\sigma(\pi^+, p)$ (mb) | $\sigma(p, p)$ (mb) |
|---|---|---|
| 1.42 | 39.5 ± .50 | $46.2^{+0.5}_{-0.45}$ |
| 1.60 | 36.5 ± .97 | $47.5^{+1.02}_{-0.61}$ |
| 1.73 | 30.3 ± .42 | $46.2^{+0.82}_{-0.46}$ |
| 1.89 | 29.0 ± .75 | $46.8^{+1.51}_{-0.68}$ |
| 2.05 | 28.3 ± .63 | $45.3^{+1.12}_{-0.47}$ |
| 2.47 | 29.2 ± .57 | $45.1^{+0.83}_{-0.45}$ |
| 2.97 | 29.5 ± .53 | $44.5^{+0.46}_{-0.42}$ |
| 3.58 | 28.6 ± .46 | 43.2 ± 0.43 |
| 4.00 | 27.8 ± .53 | 41.6 ± 0.65 |

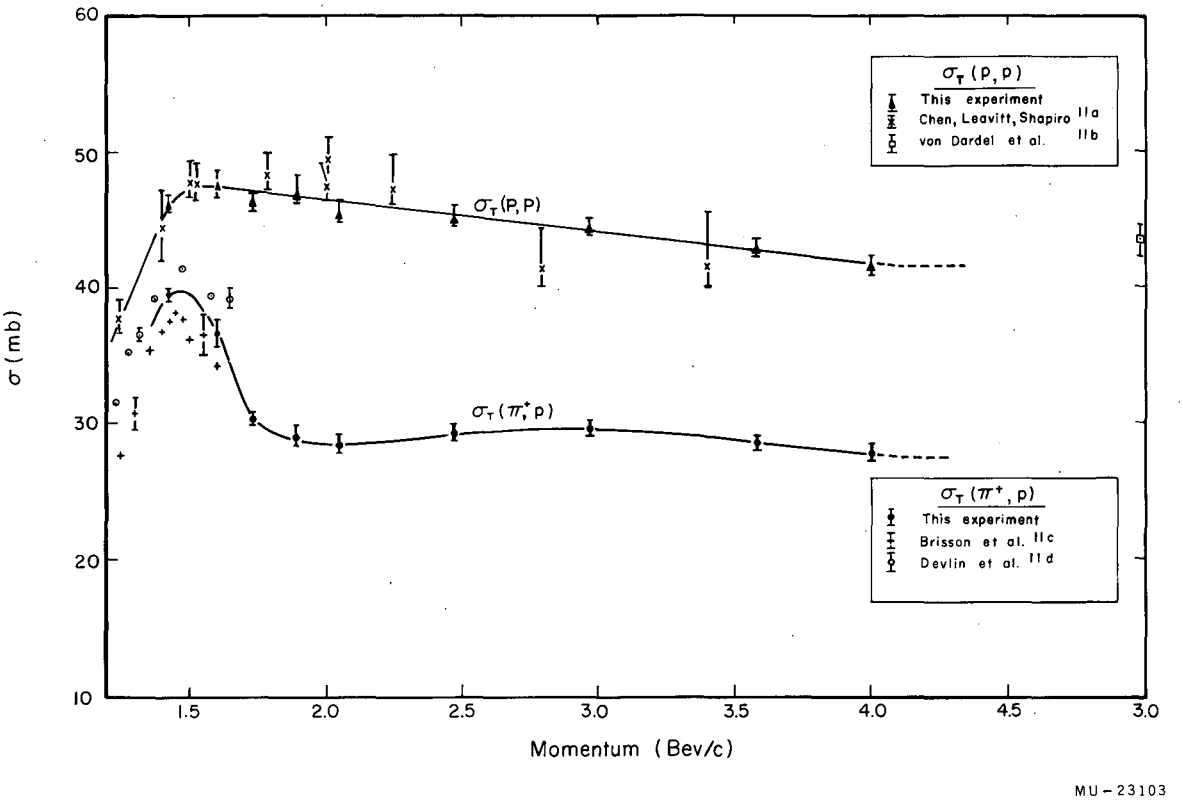


Fig. 8. Total $\pi^+$-p and p-p cross sections.

## B. Cross Sections for Positive Pions and Protons on Be, C, Al, and Cu at 3.0 Bev/c

The measured cross sections for 3.0-Bev/c pions and protons are given in Table III as a function of $\Delta\Omega$, the solid angle subtended by the transmission counter as seen from the center of the absorber. The estimated errors are also indicated. The minimum values of $\Delta\Omega$ were such that corrections for multiple Coulomb scattering were negligible, and the maximum values were such that most of the diffraction scattering was included in the cone subtended by the counter.

Some of the beryllium measurements were made with two different absorber thicknesses as a check on the method. The results are listed separately in Table III, but the two sets of measurements were combined when the data were fitted.

The pion cross sections have been corrected for muon and electron contamination as described in Sec. III. E.

Table III. Heavy-element cross sections at 3.0 Bev/c.

| Run | ΔΩ (msterad) | $\pi^+$ σ (mb) | $\pi^+$ Δσ (mb) | p σ (mb) | p Δσ (mb) |
|---|---|---|---|---|---|
| | | Beryllium (16.5 g/cm$^2$) | | | |
| 1 | 1.64 | 226.9 | 4.40 | 283.3 | 1.82 |
| 1 | 3.09 | 215.7 | 3.90 | 265.3 | 1.64 |
| 1 | 3.91 | 209.0 | 3.30 | 258.3 | 1.61 |
| 2 | 5.26 | 197.5 | 5.96 | 252.4 | 1.62 |
| 2 | 10.47 | 180.3 | 6.45 | 224.4 | 1.47 |
| 2 | 14.11 | 167.5 | 5.59 | 212.4 | 1.38 |
| 3 | 11.54 | 178.0 | 1.97 | 221.2 | 1.52 |
| 3 | 24.5 | 154.7 | 2.01 | 186.3 | 1.50 |
| 3 | 35.6 | 141.6 | 1.61 | 171.9 | 1.48 |
| | | Beryllium (8.24 g/cm$^2$) | | | |
| 1 | 5.26 | 199.9 | 4.88 | 252.9 | 4.70 |
| 1 | 10.47 | 181.2 | 4.54 | 223.5 | 5.58 |
| 1 | 14.11 | 171.9 | 4.53 | 211.8 | 4.48 |
| | | Carbon (17.1 g/cm$^2$) | | | |
| 1 | 1.64 | 267.9 | 3.85 | 341.2 | 2.66 |
| 1 | 3.09 | 247.4 | 4.10 | 312.4 | 3.50 |
| 1 | 3.91 | 235.7 | 3.60 | 302.0 | 3.18 |
| 2 | 5.26 | 237.7 | 2.78 | 297.7 | 2.24 |
| 2 | 10.47 | 210.0 | 2.00 | 257.5 | 1.82 |
| 2 | 14.11 | 195.1 | 2.78 | 242.8 | 1.63 |
| 3 | 11.54 | 216.7 | 7.25 | 265.0 | 6.30 |
| 3 | 24.5 | 193.9 | 12.5 | 224.9 | 5.80 |
| 3 | 35.6 | 176.2 | 6.73 | 210.9 | 4.50 |
| | | Aluminum (12.0 g/cm$^2$) | | | |
| 1 | 1.49 | 542. | 12.2 | 658. | 7.6 |
| 1 | 2.80 | 488. | 14.7 | 582. | 8.4 |
| 1 | 3.92 | 447. | 12.2 | 542. | 6.9 |
| 2 | 5.61 | 439. | 14.0 | 504. | 6.8 |
| 2 | 11.39 | 386. | 17.4 | 431. | 8.8 |
| 2 | 19.5 | 355. | 14.6 | 400. | 6.3 |
| | | Copper (6.80 g/cm$^2$) | | | |
| 1 | 1.49 | 1009. | 34.3 | 1209. | 10.0 |
| 1 | 2.80 | 832. | 36.6 | 986. | 9.9 |
| 1 | 3.52 | 772. | 34.7 | 947. | 8.6 |
| 2 | 2.29 | 900. | 27.0 | 1091. | 8.8 |
| 2 | 4.41 | 724. | 34.2 | 909. | 13.8 |
| 2 | 5.66 | 716. | 26.1 | 881. | 7.8 |

# V. OPTICAL-MODEL ANALYSIS OF THE NUCLEAR CROSS SECTIONS

## A. General Description of the Optical Model

By "optical model" we mean that model in which the nucleus is represented by a potential well. This potential may have both a real and an imaginary part as well as spin-orbit terms, though the latter are not considered here. With this description, the many-body problem of a particle scattering on a nucleus is replaced by a soluble two-body interaction. Most of the theoretical work along these lines has been directed toward justifying this approach and calculating these potentials, starting with a knowledge of the more fundamental interaction with individual nucleons. The line of attack depends in large measure on the energy range involved. Here we are primarily concerned with high energies (above approx 100 Mev). In this region the theory has been particularly successful in treating the interactions of pions with nuclei.

For a given particle incident on a nucleus it can be shown that the optical potential integrated over the nuclear volume is proportional to the forward amplitude for scattering by free nucleons (as averaged over all the nucleons in the nucleus). The fundamental requirement for the validity of this result is that the interaction energy $W(\vec{r})$ of a particle with a nucleus can be written in the form

$$W(\vec{r}) = \sum_{i=1}^{A} v_i(\vec{r}) , \tag{7}$$

where $v_i$ is the interaction energy of the particle with the ith nucleon when that nucleon is removed from the nucleus.

This proportionality between the integrated optical potential and the forward scattering amplitude is readily seen to be true in the Born approximation, though it can be proved on much more general assumptions.[12] In the Born approximation the forward scattering amplitude $f(0)$ for a particle incident on a single nucleon represented by a

potential $v_i(\vec{r})$ is given by

$$f(0) = -(\mu/2\pi) \int v_i(\vec{r})\, d^3r, \tag{8}$$

where $\mu$ is the reduced mass of the incident particle.* The first-order optical potential $W$ for a nucleus is obtained by "smoothing out" that due to the individual nucleons; thus

$$\int_{\substack{\text{nuclear}\\\text{volume}}} W(\vec{r})\, d^3r = \sum_{i=1}^{A} \int_{\substack{\text{nuclear}\\\text{volume}}} v_i(\vec{r})\, d^3r. \tag{9}$$

Using Eq. (8), we have

$$\int W(\vec{r})\, d^3r = -\sum_{i=1}^{A} \frac{2\pi}{\mu} f_i(0) = -\frac{2\pi A}{\mu}\left[Z/A\, f_p(0) + (1-Z/A)\, f_n(0)\right], \tag{10}$$

where $f_p(0)$ and $f_n(0)$ are the center-of-mass amplitudes for scattering by protons and scattering by neutrons, respectively. The optical potential in this approximation is proportional to the density of nucleons at that point in the nucleus. For a given density distribution, the potential as a function of position can therefore be obtained from Eq. (10).

Equation (10) holds for both the real and imaginary parts of the potential. The imaginary part is related to the total cross section for free nucleons $\sigma_T$ by the well-known relation

$$\mathrm{Im}\left[f(0)\right] = \frac{k}{4\pi}\, \sigma_T, \tag{11}$$

*Nonrelativistically, $\mu = \frac{M}{m+M}\, m$, where $m$ is the mass of the incident particle and $M$ the nucleon mass. The relativistic expression is (Ref. 13) $\mu = ME_0/E_T^*$ where $E_T^*$ is the total energy in the pion-nucleon (or proton-nucleon) center-of-mass system and $E_0$ is the total energy of the incident particle in the laboratory system.

where k is the momentum of the pion in the π-nucleon center-of-mass system.

For pion scattering it is possible to calculate the real part of the forward scattering amplitude from dispersion relations, Eq.(1). In this case, therefore, both the real and imaginary parts of the first-order optical potential are well known.

Equation (10) must be corrected to take into account the effects of the Pauli exclusion principle, which can raise or lower the effective potentials depending on the energy of the incident particle. At low energies it acts to inhibit collisions with small momentum transfers, thus decreasing the potentials (in absolute value). At high energies this effect is small and is overshadowed by another which tends to increase the optical potentials. The latter is the mutual repulsion of nucleons at small distances, which keeps them apart and makes them more effective as scattering targets. At 3.0 Bev/c the over-all effect is an increase in the potentials of approximately 15%.

For small nuclei, Eq. (10) must be further corrected for terms of order 1/A which appear in a more careful derivation. These terms do not appear in the Born approximation, and we shall hopefully neglect them. We shall also neglect a correction to the pion-nucleus potentials due to the possibility of direct absorption by two or more nucleons in the nucleus in reactions of the type $\pi^+ + p + n \rightarrow p + p$. These reactions are important at low energies but are not expected to play a significant role at 3.0 Bev/c. Corrections to the proton-nucleus potentials due to the identity of the incident and target particles are also expected to be small.[14]

## B. Calculation of the Optical Potentials from the Interaction with Free Nucleons

### 1. Pion-Nucleus Scattering

From Eq. (10) the integrated optical potential is, to first order,

$$\frac{1}{A}\int W(\vec{r})\, d^3r = -\frac{2\pi}{M}\frac{E_T^*}{E_0}\left[\frac{Z}{A} f_p(0) + \left(1-\frac{Z}{A}\right) f_n(0)\right]. \qquad (11a)$$

For positive pions, we have $f_p \equiv f(\pi^+, p)$, and $f_n \equiv f(\pi^+, n) = f(\pi^-, p)$ by charge symmetry.

Cronin has used the total cross sections of this and other experiments to calculate from dispersion relations the real parts of the forward scattering amplitudes for pion scattering.[15] Extrapolating his results slightly to 3.0 Bev/c and transforming to the c.m. system, we have

$$\mathcal{R}e\left[f(\pi^+, p)\right] = -0.095; \quad \mathcal{R}e\left[f(\pi^-, p)\right] = -0.26 \text{ fermi.}$$

Using $\sigma_T(\pi^+, p) = \sigma_T(\pi^-, p) = 2.9 \text{ fermi}^2$, we have

$$\mathcal{I}m\left[f(\pi^+, p)\right] = \mathcal{I}m\left[f(\pi^-, p)\right] = \frac{k}{4\pi}\,\sigma_T = 1.29 \text{ fermi.}$$

This yields for $Z/A \approx 1/2$ the first-order potential

$$\frac{1}{A}\int W^{(1)}(r)\, d^3r = (39.5 - 286\, i)\ \text{Mev-fermi}^3. \tag{12}$$

The real part of the potential is therefore small and repulsive.

The first-order potentials must be corrected for nuclear correlation brought about by the effects of the exclusion principle. According to Watson and Zemach,[16] the optical potential correct to second order is

$$W^{(2)} = \left(U^{(1)} - i\,|V^{(1)}|\right)(1 + i\,\Delta_R + \Delta_I), \tag{13}$$

where $U^{(1)} - i\,|V^{(1)}|$ is the first-order potential, and for $\beta \approx 1$, we have

$$\Delta_R = -U^{(1)} R_c; \quad \Delta_I = -|V^{(1)}|\, R_c. \tag{14}$$

The correlation length $R_c$ is a measure of the correlation of nucleon positions in the nucleus. Its value can be calculated for particular

models of the nucleus. For a degenerate Fermi gas model, $R_c \approx -0.4$ fermi.[16] (Negative values of $R_c$ correspond to an over-all repulsive interaction.) Using the Brueckner model, we get $R_c \approx -0.63$ fermi.[17] We shall use the latter value. From Eq. (12), assuming a square-well potential of radius $1.2\ A^{1/3}$, we find $U^{(1)} = +5.5$, $|V^{(1)}| = 39.5$. This yields $\Delta_R = -0.02$ and $\Delta_I = +0.125$, and the integrated optical potential for pions, correct to second order, is

$$\frac{1}{A}\int W^{(2)}(\vec{r})\,d^3r = (38.8 - 323i)\ \text{Mev-fermi}^3. \qquad (15)$$

2. Calculation of the Proton-Nucleus Optical Potentials

For p-p and p-n scattering little is known about the real part of the forward scattering amplitudes at high energies. The most accurate data seem to be those of Preston, Wilson, and Street,[18] who find, at 3.8 Bev/c,

$$|\mathrm{Re}[f(p,p)]| \lesssim 0.1 \cdot |\mathrm{Im}[f(p,p)]|.$$

Barashenkov and Nen-ning,[19] on the other hand, conclude that

$|\mathrm{Re}[f(p,p)]| \approx 0.49 \cdot |\mathrm{Im}[f(p,p)]|$ at 3.0 Bev/c, and

$|\mathrm{Re}[f(p,p)]| \approx 0.31 \cdot |\mathrm{Im}[f(p,p)]|$ at 5.3 Bev/c. We therefore assume, for <u>both</u> p-p and p-n scattering, $|\mathrm{Re}f| \approx \frac{1}{5}|\mathrm{Im}f|$.

Using $\sigma_T(p,p) = 44.5$ mb at 3.0 Bev/c from Table III and $\sigma_T(n,p) = 41.5$ mb,[20] we obtain from Eq. (10a)

$$\frac{1}{A}\int W^{(1)}(\vec{r})\,d^3r = (\pm 80 - 400\,i)\ \text{Mev-fermi}^3,$$

where the sign of the real part of the potential is uncertain. If we assume that Eqs. (13) and (14) for the second-order potentials are correct

for protons as well as pions, then, neglecting $\Delta_R$, we have

$$\frac{1}{A}\int W^{(2)}(r)\, d^3r = (\pm 94 - 470\, i)\ \text{Mev-fermi}^3 \qquad (16)$$

for $Z \approx A/2$.

C. The Method Used in Fitting the Experimental Data

1. The Shape of the Potential Well

In fitting the experimental data a process of trial and error was used. A potential well was chosen, and cross sections calculated. These cross sections were compared with the experimental ones, and the process repeated until good fits were obtained.

In this method it is necessary to assume a shape for the nuclear potential well. In the past a square-well potential was usually chosen to simplify calculations. This shape, however, is quite unrealistic and generally leads to unsatisfactory agreement with experiment.[21] Data from electron-scattering experiments are consistent with a nuclear density distribution having a Fermi shape.[22] Since the shape of the optical potential is expected to resemble that of the nuclear density distribution, a Fermi well was used in fitting the data of this experiment. It was further assumed that both the real and imaginary parts of the potential have the same shape. The potential $W(r)$ therefore has the form

$$W(r) = U(r) + i\, V(r) = \frac{U_0 + i\, V_0}{1 + e^{(r-r_0)/a}}\ , \qquad (17)$$

where $r_0$ is the radius at which the potential drops to $(U_0 + i\, V_0)/2$ and $a$ is a parameter which determines the rate of falloff. For $a \ll r_0$, the well is almost "square."

In the initial attempts to fit the data it became apparent that good fits could be obtained over a wide range of values of the parameters $U_0$, $V_0$, $r_0$, and $a$, if all were allowed to vary. Increasing

$r_0$ could be compensated for by decreasing $U_0$ and $V_0$; decreasing a could be compensated by decreasing $U_0$ with respect to $V_0$. It was therefore decided to fix $r_0$ and a at the values obtained in the electron-scattering experiments. The values used are listed in Table IV, which also lists the values of $U_0$ and $V_0$ that yield the integrated potentials of Eqs. (15) and (16). The electron-scattering data for beryllium were fitted with a modified exponential density distribution;[22] however, it was found that this could be well approximated by a Fermi distribution with a suitable choice of $r_0$ and a. Figure 9 shows $U(r)/U_0$ for the potential distributions used in fitting the data. The modified exponential shape used in fitting the beryllium electron-scattering data is also shown. Note that for beryllium $U(r)$ must be multiplied by $(0.62)^{-1}$ to normalize $U(r)/U_0$ to unity at the origin,

Table IV. Well parameters and predicted potentials.

| Nucleus | $r_0$ | a | $\langle r^2 \rangle^{1/2}$ | Pions | | Protons | |
|---|---|---|---|---|---|---|---|
| | | | | $U_0$(Mev) | $V_0$(Mev) | $U_0$(Mev) | $V_0$(Mev) |
| Be | 0.429 | 0.84 | 3.03 | 16.5 | -137.6 | ±40 | -200 |
| C | 2.25 | 0.45 | 2.41 | 7.0 | -58.1 | ±17 | - 85 |
| Al | 3.01 | 0.60 | 3.22 | 6.6 | -54.9 | ±16 | - 80 |
| Cu | 4.26 | 0.53 | 3.84 | 6.6 | -54.9 | ±16 | - 80 |

2. The Computer Program Used in Calculating the Optical-Model Cross Sections

The program used to calculate the cross sections is a modification of that described by Bjorklund, Blandford, and Fernbach.[23] The original version of this program solves the Schrödinger equation for a complex nuclear potential plus a Coulomb potential corresponding

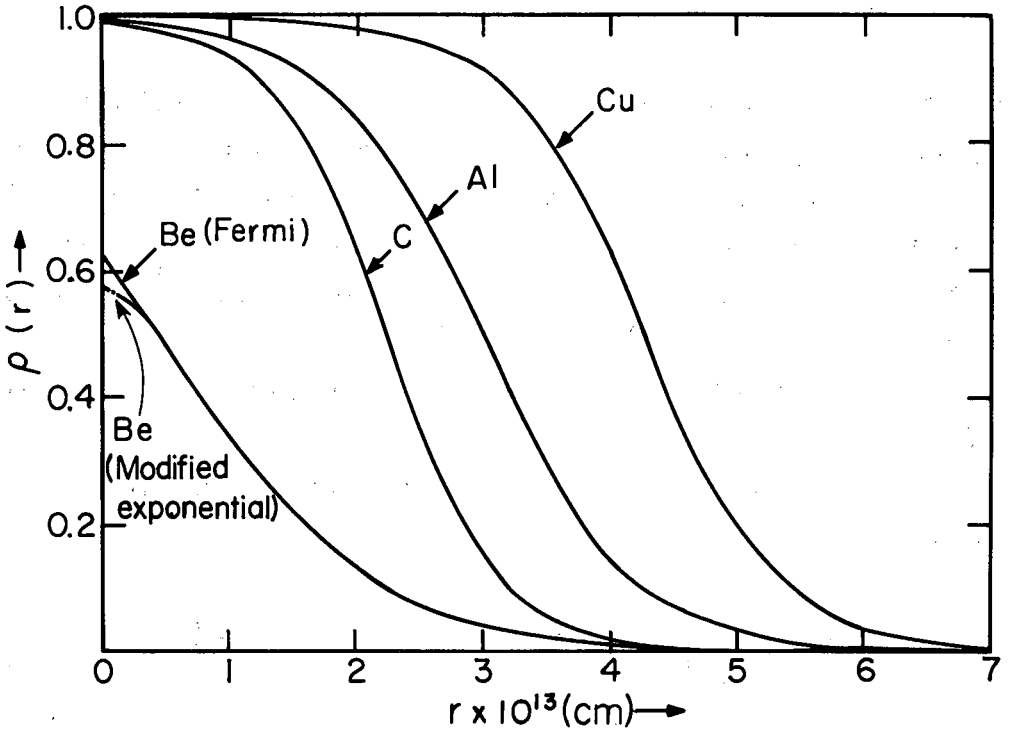


Fig. 9. Form factors for potential wells used in fitting data, $\rho(r) = [1 + e^{(r-r_0)/a}]^{-1}$.

to a nucleus with a uniform charge distribution of radius $r_0$.

$$U_{Coul} = \frac{Ze^2}{2r_0}\left[3 - \left(\frac{r}{r_0}\right)^2\right] \quad \text{for } r < r_0, \tag{18}$$

$$U_{Coul} = \frac{Ze^2}{r} \quad \text{for } r > r_0 .$$

The resulting wave equation must be integrated numerically for each angular momentum state. The complex phase shifts are then determined by matching the resulting wave functions to Coulomb wave functions at the edge of the nucleus. The differential cross sections for scattering at any angle and the total inelastic cross sections can then be calculated.

The original version was modified to treat relativistic particles as follows:

(a) The original program solved the radial Schrödinger equation,

$$\left[-\frac{1}{r^2}\frac{d}{dr}\left(r^2\frac{d}{dr}\right) + \frac{\ell(\ell+1)}{r^2}\right] R = 2m\left[T - W(r)\right]R. \tag{19}$$

It was assumed that the scattering of both pions and protons could be described by the Klein-Gordon equation,[24]

$$\left[-\frac{1}{r^2}\frac{d}{dr}\left(r^2\frac{d}{dr}\right) + \frac{\ell(\ell+1)}{r^2}\right] R = \left[(E - W(r))^2 - m^2\right]R. \tag{20}$$

Actually, the Dirac equation is the proper wave equation for protons; however, if spin effects are neglected the Dirac equation reduces to the Klein-Gordon equation.[25] Neglecting terms in $(W/E)^2$ compared to unity, we can rewrite Eq. (20) as

$$\left[-\frac{1}{r^2}\frac{d}{dr}\left(r^2\frac{d}{dr}\right) + \frac{\ell(\ell+1)}{r^2}\right] R = \left[p^2 - 2EW(r)\right]R, \tag{20a}$$

where $p^2 = E^2 - m^2$. Equation (20a) has the same form as Eq. (19) with $2mT$ replaced by $p^2$ and $M$ replaced by $E$.

(b) The original version had to be modified to treat problems in which angular momentum states with $\ell \approx 100$ were important. The relativistic version allows $\ell_{max} < 200$. Running time for the 3.0-Bev/c problems was 10 to 20 minutes.

As a check on the new version, another program was written independently to calculate the scattering by a real "square well" using analytical solutions. A comparison of the two programs for 3.0-Bev/c pions showed agreement to approx 0.2% when the falloff parameter a was made small in the Fermi-well case to approximate a square well.

3. The Method Used in Comparing the Calculated Cross Sections with the Experimental Data

If we neglect the finite angular resolution of the counter telescope,* it is expected that the measured cross section $\sigma(\theta)$ will have the following dependence on $\theta$, the angle subtended by the edge of the transmission counter (see Fig. 1):

$$\sigma(\theta) = \int_{\theta' = \theta}^{\theta' = \pi} \frac{d\sigma_{el}(\theta')}{d\Omega'} \, d\Omega' + \sigma_a - 2\pi \eta (1 - \cos\theta). \qquad (21)$$

The first term is the cross section for elastic scattering at angles greater than $\theta$; the second represents the loss of particles due to all inelastic processes (absorption). The third term is due to inelastic events which give rise to charged secondary particles that count in the transmission counter, thus lowering the apparent cross section. We assume that for angles at which measurements were made ($0 < \theta < 6$ deg) the differential cross section for producing charged secondaries, $\eta$, is approximately constant, so that this term is proportional to the solid

*The actual case in which the resolution is taken into account is treated in Appendix II. This method of fitting the data is similar to that used by Cronin, Cool, and Abashian (Ref. 26).

angle subtended by the transmission counter, $2\pi(1-\cos\theta)$. The proportionality constant $\eta$ was determined for each pair of $U_0$ and $V_0$ by a least-squares fit to the data with the restriction that $\eta$ be positive.

In fitting the experimental data to the functional form given in Eq. (21), all calculations were carried out in the center-of-mass system of the incident particle and the target nucleus. This merely involved transforming the angle $\theta$ to its corresponding angle in the center-of-mass system, $\theta^*$.

For each pair of $U_0$ and $V_0$, a value of $\chi^2$ was determined, where

$$\chi^2 = \sum_{i=1}^{N} \left[ \frac{\sigma^i_{meas} - \sigma^i_{calc}}{\Delta\sigma_{meas}} \right]^2 . \qquad (22)$$

For a "good fit," $\chi^2$ is approximately equal to the number of experimental points minus the number of fitted parameters or, in this case, N - 3 (corresponding to the three fitted parameters $V_0$, $U_0$, and $\eta$).

## D. The Results of the Analysis: The Best-Fit Values of the Potentials

Figures 10 through 17 show plots of $\chi^2$ vs $V_0$ for various values of $U_0$. Only positive (repulsive) values of $U_0$ are shown. The plots for negative real potentials are quite similar.* Several conclusions can be drawn immediately from these graphs:

*In making these plots, cross sections were calculated exactly only at several values of $V_0$ near the minimum in $\chi^2$ for each $U_0$, in order to conserve computer time. Cross sections at near-by values of $V_0$ were then determined by interpolation, and the interpolated cross sections were used to calculate $\chi^2$ as a function of $V_0$. The error involved in this procedure was found by repeated tests to be negligible.

1. The values of $U_0$ that best fit the experimental data are much larger than the predicted values given in Table IV. In most cases, however, the fits are not sensitive to $U_0$, especially when $U_0$ is small.

2. The minimum values of $\chi^2$ in some cases are widely different from the expected values ($\approx 6$ for Be and C, and $\approx 3$ for Al and Cu). This may be partially due to assigning to the experimental points errors that are too large or too small. Also, since the experimental cross sections were measured at three values of $\theta$ at a time, there may be some correlation in their errors. This would cause a deviation from the expected distribution of $\chi^2$. (The small fluctuations in the experimental data that were discussed in Section III. F were such that all three points measured during one run were raised or lowered together.)

3. If $U_0$ is fixed, $V_0$ is well determined; but if $U_0$ is allowed to vary, the range of acceptable $V_0$ is rather large.

The discrepancy between the best-fit values of $U_0$ and the predicted ones is further illustrated in Figs. 18 and 19. These show the minimum value of $\chi^2$ for each $U_0$ plotted vs $U_0$. The predicted values of $U_0$ from Table IV are indicated by arrows. It can be seen that in most cases the large values of $U_0$ are only slightly favored statistically over the predicted ones.

The magnitude of the discrepancy is more clearly demonstrated in Figs. 20 and 21, which compare the experimental cross sections with the calculated ones for $U_0 \approx 0$ (the predicted value) and also for the best-fit value of $U_0$. The two cases illustrated (pions on Be in Fig. 20, and protons on Al in Fig. 21) are ones in which the high values of $U_0$ are most favored statistically. The discrepancy could be removed completely if the cross sections at intermediate angles were raised approximately 2%, or if the small-angle points were lowered about the same amount. (The latter alternative would also involve readjusting the best-fit values of $V_0$ and $\eta$.)

It is therefore quite possible that this discrepancy is due to a small systematic error in the cross-section measurements or to some

deficiency in the method used in fitting the data. Possible explanations are discussed in detail in Section VI. B.

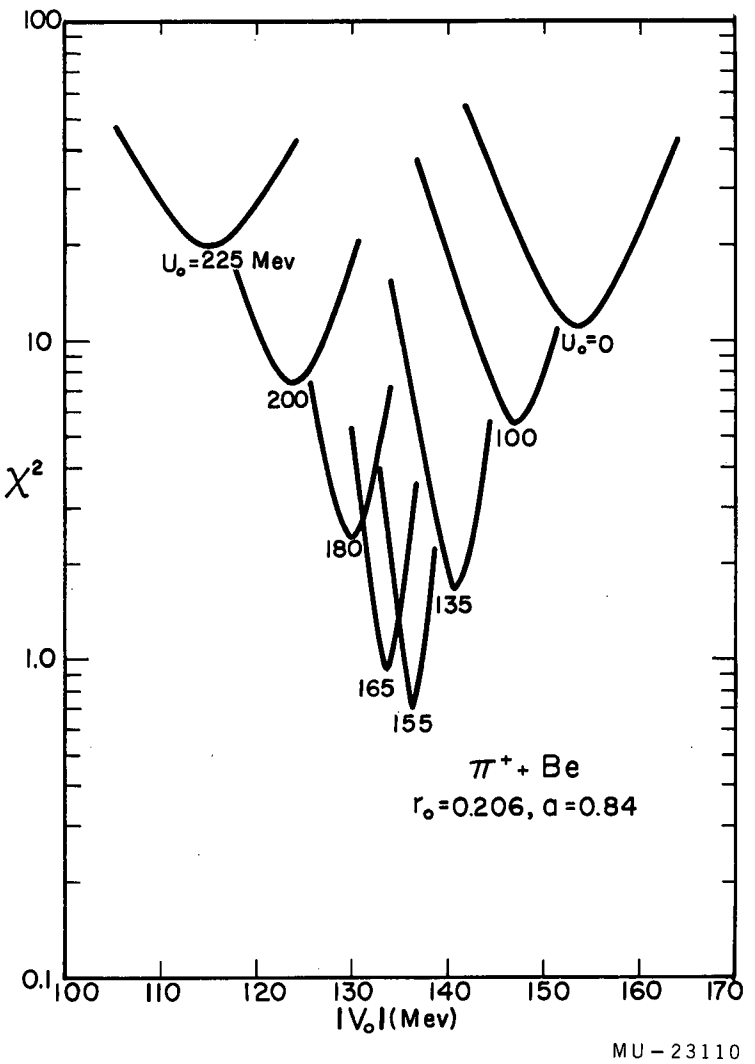


Fig. 10. $\chi^2$ vs $V_0$ for various values of $U_0$. Plots for negative values of $U_0$ are similar.

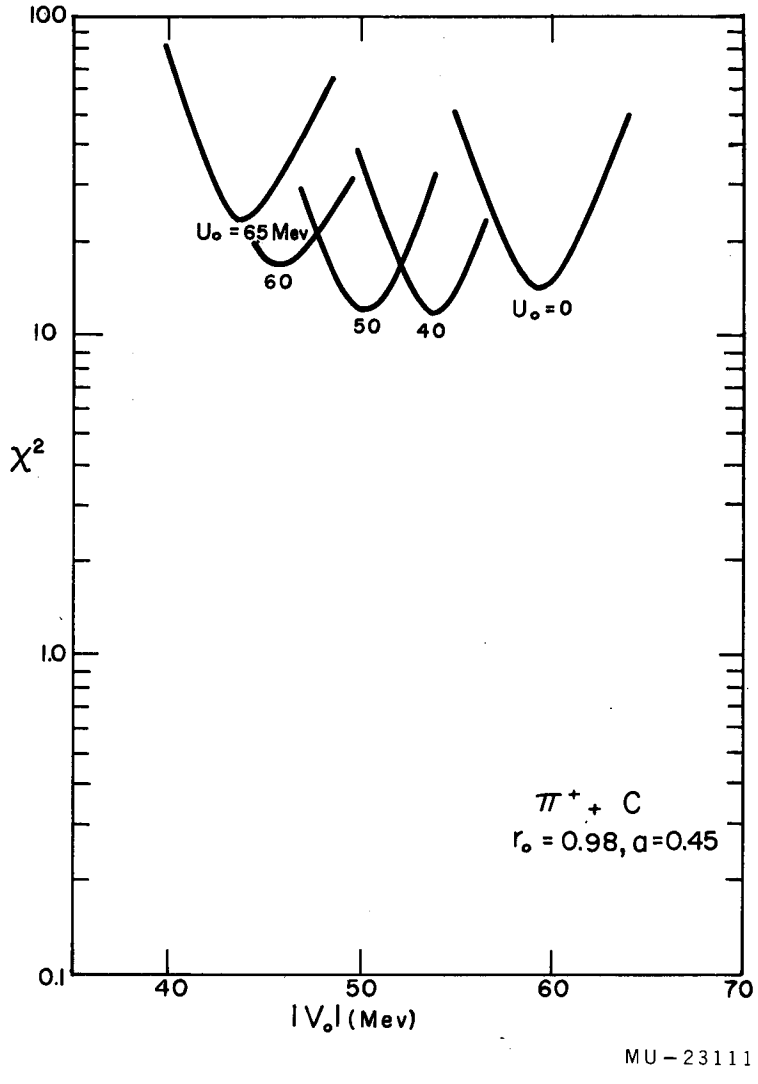


Fig. 11. $\chi^2$ vs $V_0$ for various values of $U_0$. Plots for negative values of $U_0$ are similar.

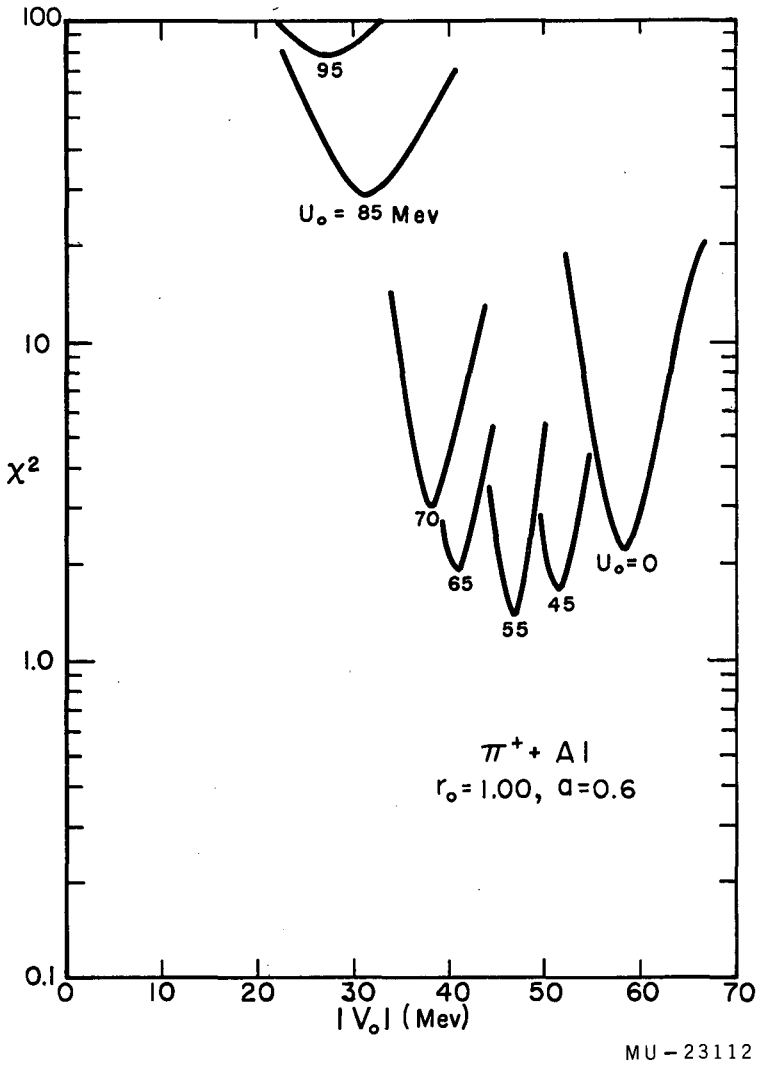


Fig. 12. $\chi^2$ vs $V_0$ for various values of $U_0$. Plots for negative values of $U_0$ are similar.

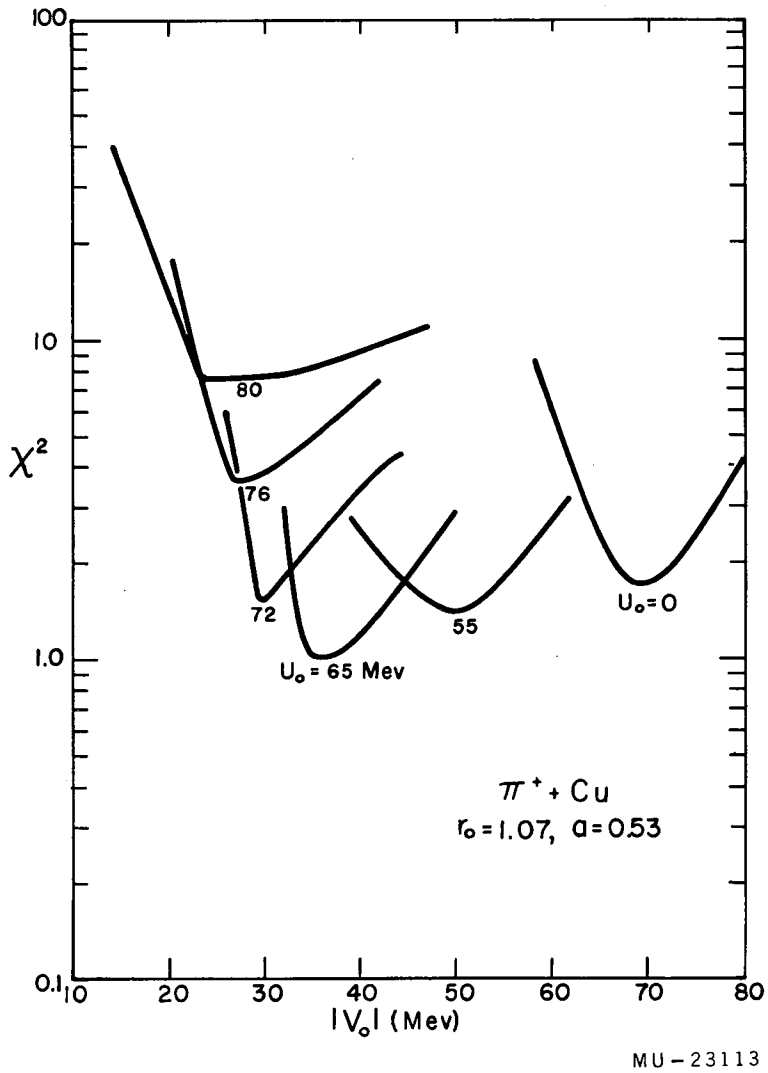


Fig. 13. $\chi^2$ vs $V_0$ for various values of $U_0$. Plots for negative values of $U_0$ are similar.

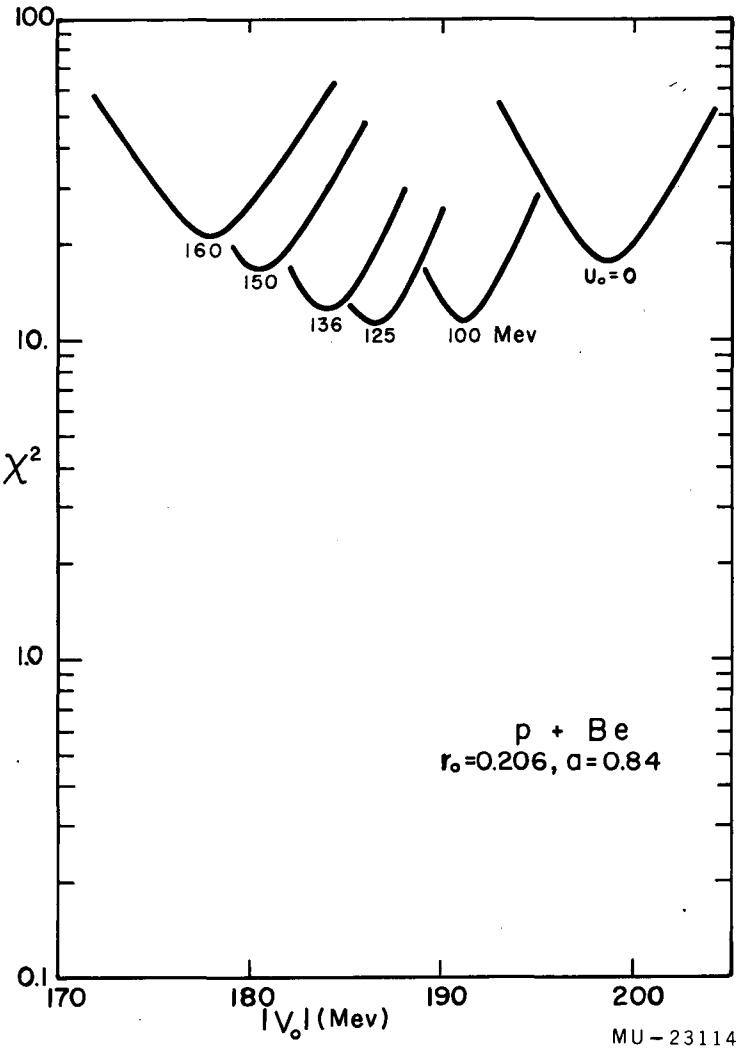


Fig. 14. $\chi^2$ vs $V_0$ for various values of $U_0$. Plots for negative values of $U_0$ are similar.

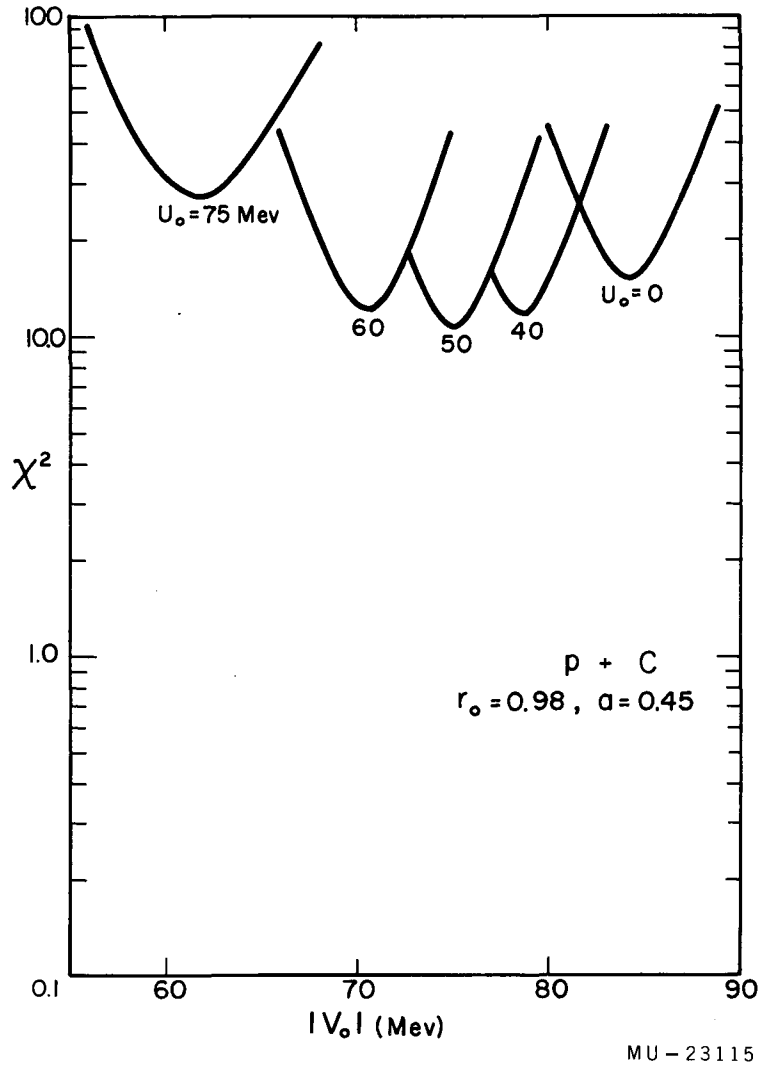


Fig. 15. $\chi^2$ vs $V_0$ for various values of $U_0$. Plots for negative values of $U_0$ are similar.

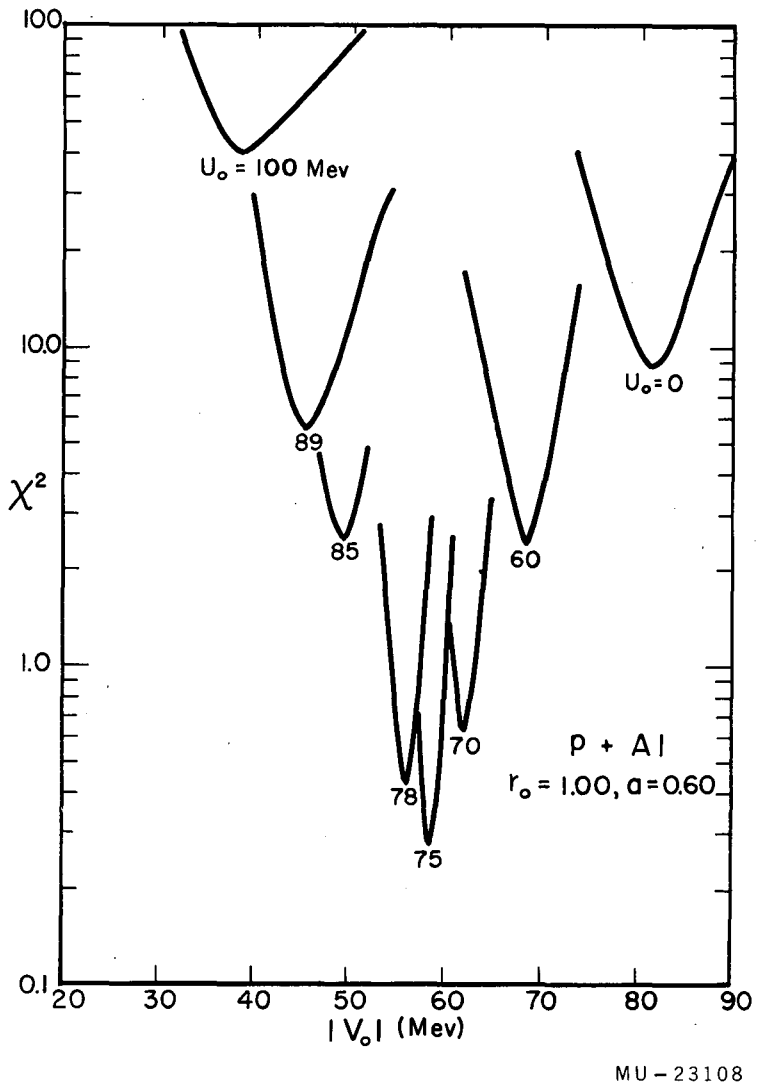


Fig. 16. $\chi^2$ vs $V_0$ for various values of $U_0$. Plots for negative values of $U_0$ are similar.

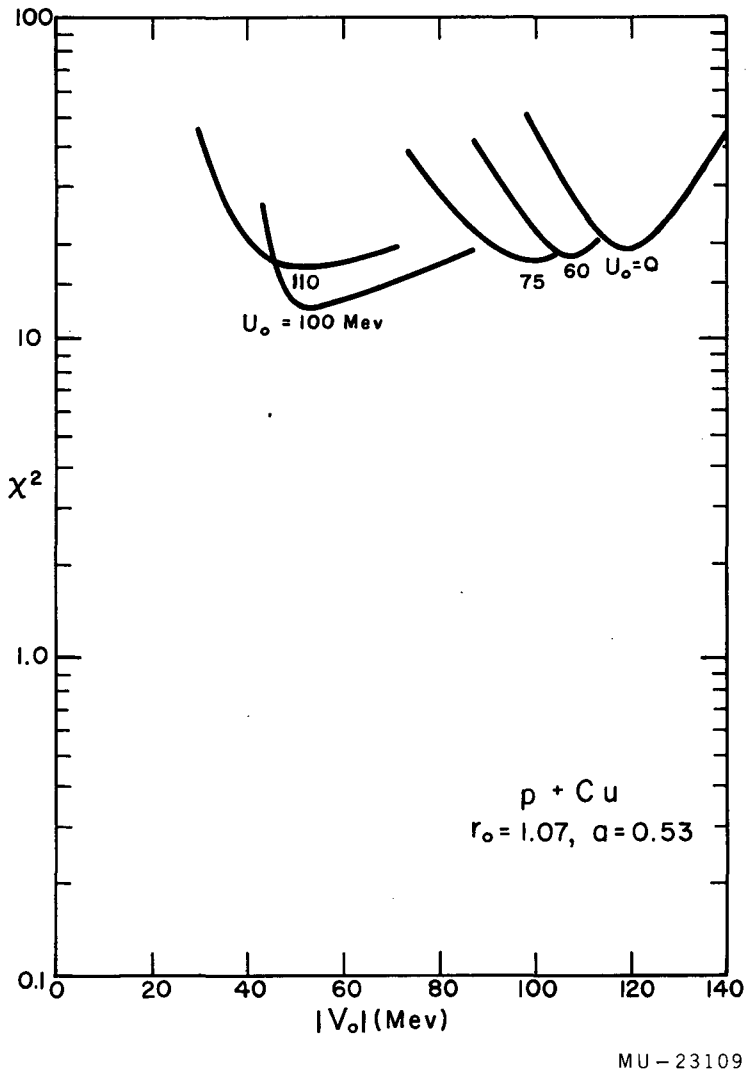


Fig. 17. $\chi^2$ vs $V_0$ for various values of $U_0$. Plots for negative values of $U_0$ are similar.

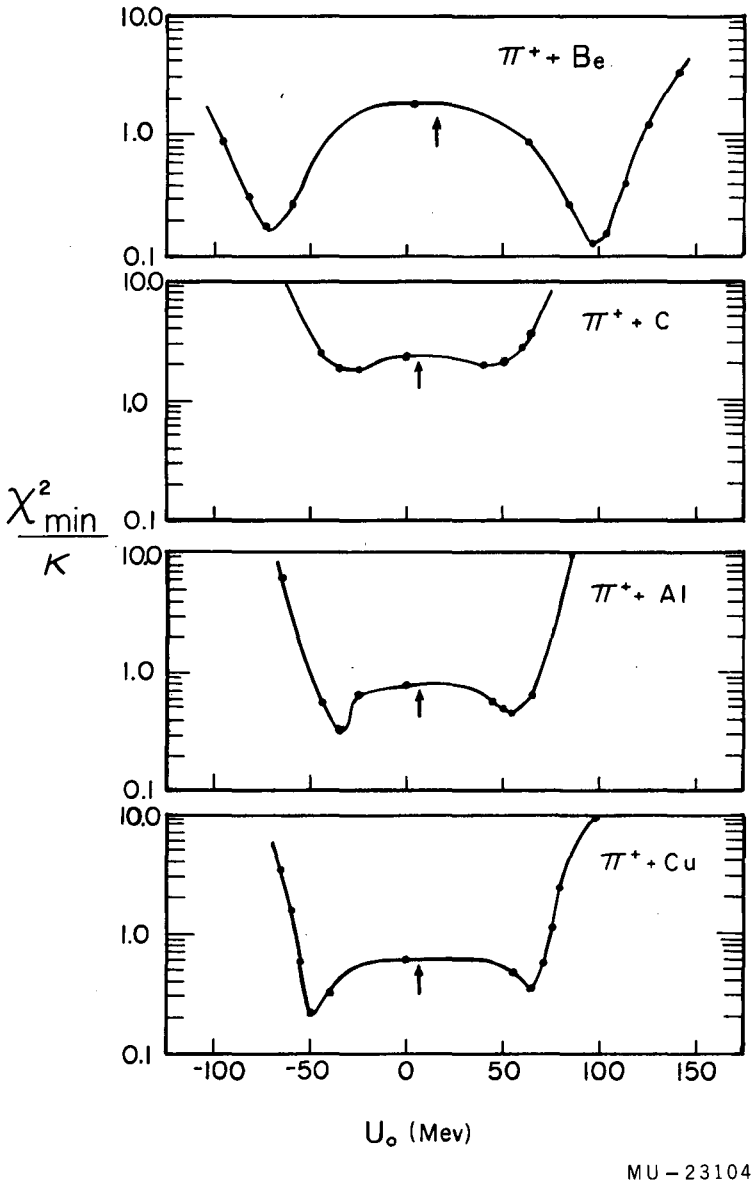


Fig. 18. The minimum values of $\chi^2/\kappa$ for each $U_0$. $\kappa$ is the number of degrees of freedom in the fit (6 for Be and C, 3 for Al and Cu). The predicted values of $U_0$ are indicated by arrows. For easier comparison with the results for other nuclei $U(r=0) = 0.62\ U_0$ is plotted for Be.

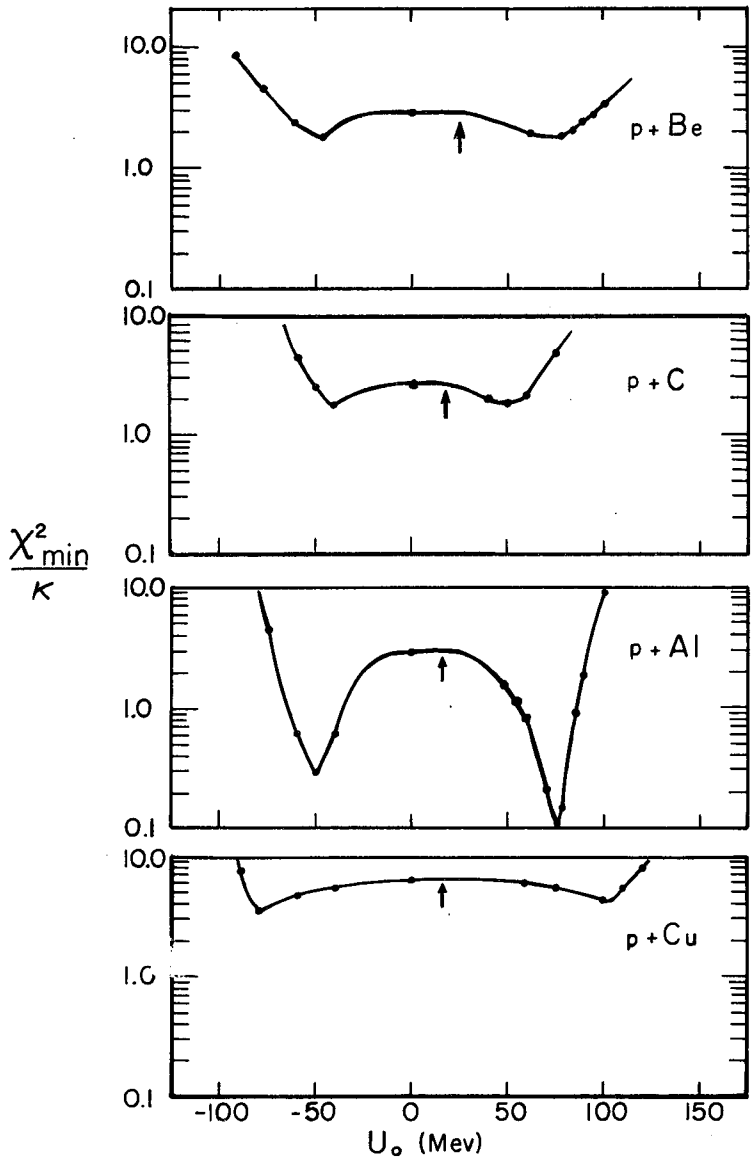


Fig. 19. The minimum values of $\chi^2/\kappa$ for each $U_0$. $\kappa$ is the number of degrees of freedom in the fit (6 for Be and C, 3 for Al and Cu). The predicted values of $U_0$ are indicated by arrows. For easier comparison with the results for other nuclei $U(r=0) = 0.62\ U_0$ is plotted for Be.

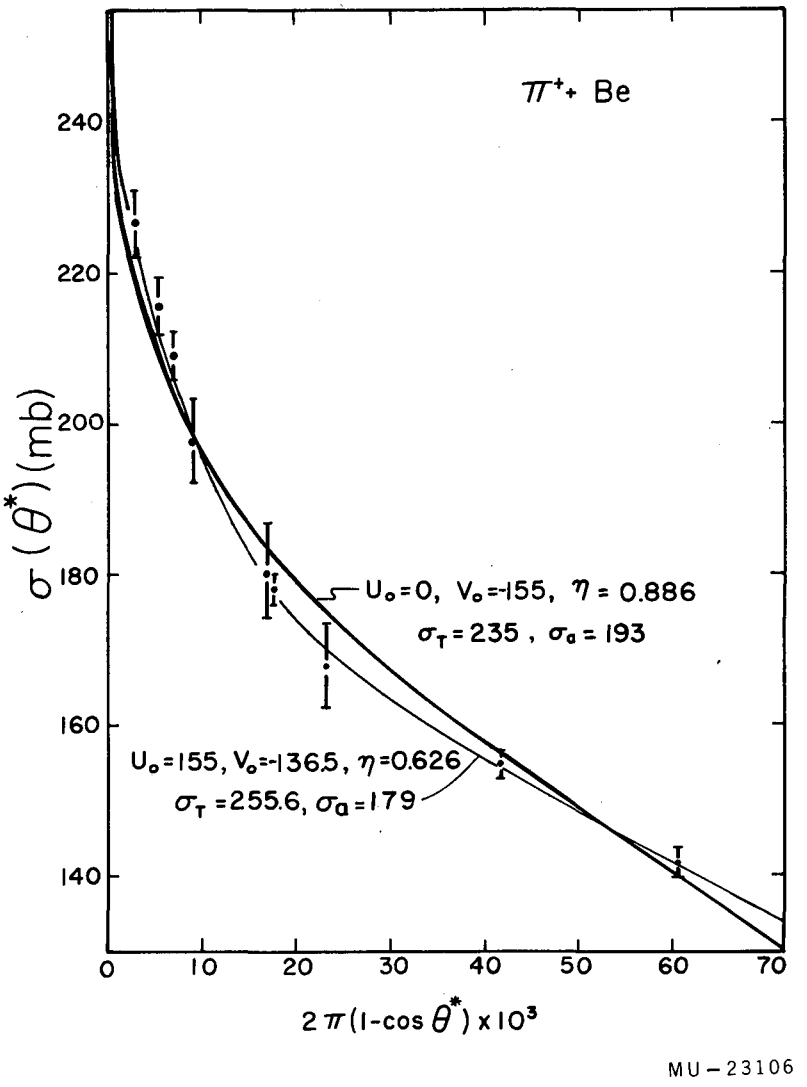


Fig. 20. Examples of fits to the experimental data. $U_0 \approx 0$ is the predicted value. $\theta^*$ is the angle in the pion-nucleus or proton-nucleus center-of-mass system.

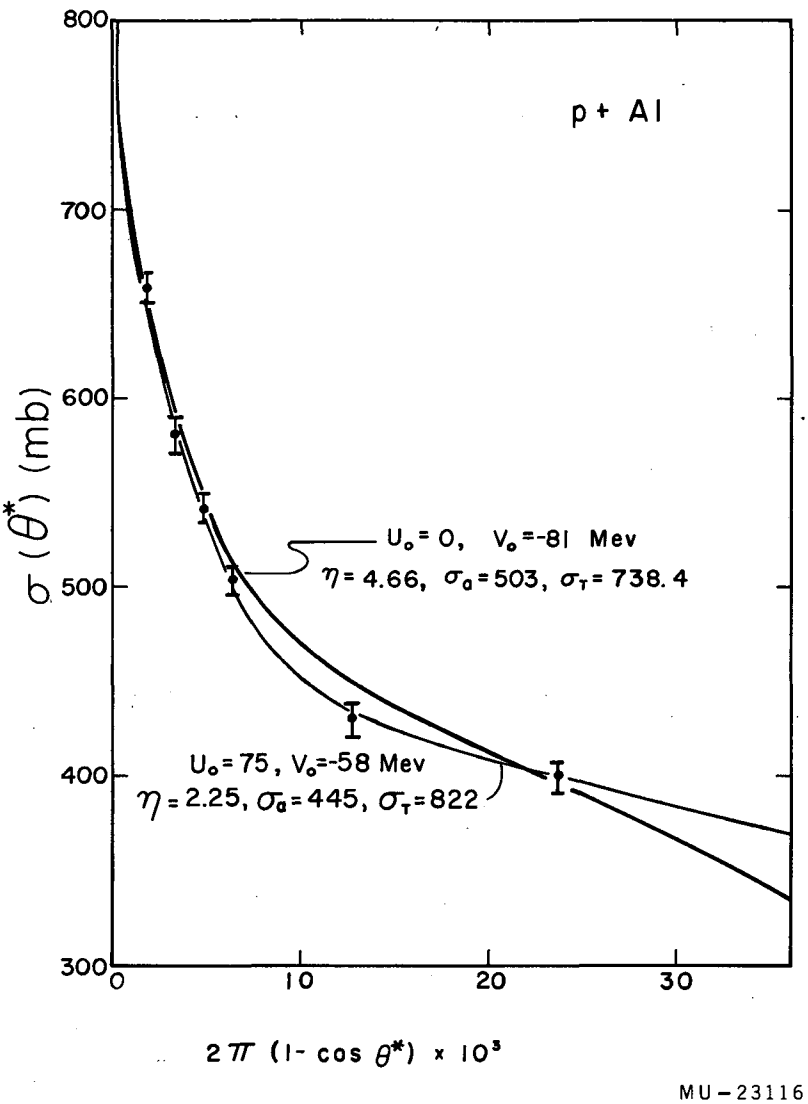


Fig. 21. Examples of fits to the experimental data. $U_0 \approx 0$ is the predicted value. $\theta^*$ is the angle in the pion-nucleus or proton-nucleus center-of-mass system.

# VI. DISCUSSION OF RESULTS

## A. The Total Cross Sections for Scattering by Hydrogen

One of the most striking aspects of the $\pi^+$-p total cross section plotted in Fig. 8 is its near constancy above 2 Bev/c. This is interesting in view of a theorem due to Pomeranchuk which states that if the total cross sections for a particle and its antiparticle on hydrogen approach constant values at high energies these limits must be equal.[27] The available data for $\pi^-$-p scattering show a similar flattening at high energies at approximately the same value.[11b] This is the best experimental evidence to date for the validity of Pomeranchuk's theorem.

The p-p cross sections in the momentum range of this experiment show no sign of approaching a constant value. At 4.0 Bev/c the $\bar{p}$-p cross section is still 30 mb higher than the p-p cross section. Recent measurements at the CERN accelerator indicate that the difference decreases to 10 mb at 10.7 Bev/c.[11b]

## B. Discussion of the Fitted Values of the Optical Potentials

The discrepancy between the best-fit experiment values of the real potential and the calculated ones is considerably outside of the uncertainty in the calculated potentials. There are several possible explanations of this result.

1. When the falloff parameter a was made smaller, good fits were obtained with considerably lower real potentials. To obtain agreement with the predicted values of $U_0$ it was necessary to reduce a almost to zero. It is quite difficult, however, to reconcile this with current theories regarding the structure of the nucleus. The variation of the best-fit values of the real potential(integrated) with $r_0$ was also studied, and it was found that the fitted values were insensitive to small changes in $r_0$.

2. The neglect of spin-orbit coupling might explain the discrepancy in the proton scattering results. Furthermore, since all of

the nuclei studied except carbon had nuclear spins,* the most general optical potential for both pions and protons includes a term proportional to $\vec{L}\cdot\vec{I}$, where $\vec{L}$ is the angular momentum of the incident particle and $\vec{I}$ the nuclear spin. Both this and the spin-orbit term, however, would be of relative order $1/A$, while the observed discrepancy does not seem to depend on A.

3. In comparing the experimental cross sections with the calculated ones as given by Eq. (21), it was assumed that $\eta$, the differential cross section for the production of charged secondaries, was constant over the range of angles studied. This assumption, though a necessary one, is open to question. Drell has in fact suggested that at high energies the production of secondary particles from inelastic collisions is strongly peaked forward at lab angles $\lesssim m/E_0$, where m is the pion mass and $E_0$ the total energy of the incident particle in the laboratory system.[28] At 3.0 Bev/c this characteristic angle is $\approx$ 3 deg.

If $\eta$ is strongly dependent on $\theta$, then Eq. (21) should be replaced by

$$\sigma(\theta) = \int_{\theta'=\theta}^{\theta'=\pi} \frac{d\sigma_{el}(\theta')}{d\Omega'}\, d\Omega' + \sigma_a - \int_{\theta'=0}^{\theta'=\theta} \eta(\theta')\, d\Omega'. \qquad (23)$$

Let us assume that $\eta(\theta')$ can be separated into two parts, one of which is essentially constant over the angular interval 0 to 6 deg and the other strongly dependent on angle:

$$\eta(\theta') = \eta_0 + \eta_1(\theta').$$

Equation (23) can then be rewritten

$$\sigma(\theta) = \int_{\theta'=\theta}^{\theta'=\pi} \left[\frac{d\sigma_{el}(\theta')}{d\Omega'} + \eta_1(\theta')\right] d\Omega' + \sigma_a - \sigma_1 - 2\pi\,\eta_0(1-\cos\theta), \qquad (24)$$

*$Be^9$ has spin I=3/2, $Al^{27}$ has spin I=5/2, $Cu^{63}$ and $Cu^{65}$ have spin 3/2.

where $\sigma_1 \equiv \int_0^{\pi} \eta_1(\theta)\, d\Omega$. The effect of the forward peaking of charged secondaries is thus to decrease the apparent absorption cross section and increase the apparent elastic cross section.* It can be seen from Figs. 20 and 21 that the magnitude of this effect need not be large to cause the observed discrepancy. A rough estimate based on Drell's calculation indicates that this forward peaking of secondary particles is large enough to explain it.

In view of the above discussion it is reasonable to conclude that the results of this experiment do not disagree with the predictions of the optical model and dispersion relations concerning the magnitude of the real part of the potential. A much more definitive test could be made if data were available on the distribution of charged secondaries at small angles, or if the differential elastic cross sections were measured directly.

Table V gives the values of $V_0$ that best fit the data when $U_0$ is restricted to be small, as theory predicts. The predicted values of $V_0$ are also shown, and the agreement is generally quite good. On the other hand, if the best-fit values of $U_0$ are adopted, then $V_0$ must be made considerably smaller than the predicted values of fit the data (Figs. 10 through 17). This lends further support to the conclusions that the best-fit values of $U_0$ are not the correct ones.

Two quantities of considerable interest are the total nuclear cross section $\sigma_T$ and the absorption cross section $\sigma_a$. For heavy nuclei it is difficult to measure the total cross section at high energies because Rutherford scattering is large over the major part of the diffraction pattern. However, once optical-well

---

*The differential cross section for quasi-elastic scattering, in which the target nucleus is left intact but in an excited state, is small at small scattering angles and increases with angle (Ref. 17). This would give a term in $\eta(\theta')$ which decreases with increasing $\theta'$. This effect, however, is expected to be small.

parameters that fit the experimental data are determined it is possible to define the total nuclear cross section in terms of these. To do this, we simply "turn off" the Coulomb interaction and calculate the total cross section for the potential well with no Coulomb potential. For light nuclei this is the same as obtained by extrapolating the measured cross sections to 0 deg, as is usually done.

Table V. Best-fit values of $V_0$ for $U_0 \approx 0$.

| | $\lvert V_0 \rvert$ Predicted (Mev) | $\lvert V_0 \rvert$ Best fit (Mev) |
|---|---|---|
| $\pi^+$+Be | 137.6 | 154. ± 9.0 |
| $\pi^+$+C | 58.1 | 59.6± 4.0 |
| $\pi^+$+Al | 54.9 | 58.5± 4.1 |
| $\pi^+$+Cu | 54.9 | $69.0^{+13.5}_{-8.0}$ |
| p+Be | 200. | 199. ± 6.0 |
| p+C | 85. | 84.3± 4.3 |
| p+Al | 80. | 81.5± 6.5 |
| p+Cu | 80. | 120. ±24. |

The absorption cross section can also be defined in terms of the best-fit parameters. The total elastic cross section $\sigma_{el}$ is then $\sigma_T - \sigma_a$. The values of $\sigma_a$ and $\sigma_{el}$ thus obtained are listed in Table VI.

The errors in the values of $V_0$ given in Table V are such that at the upper and lower limits $\chi^2$ is three times the minimum value. The upper and lower limits on $\sigma_a$ and $\sigma_{el}$ in Table VI are the values corresponding to the upper and lower limits on $V_0$.

For comparison, Table VI also lists the values of $\sigma_a$ and $\sigma_{el}$ found in other experiments with high-energy pions and nucleons. Taking into account the variations of the free-nucleon cross sections, we find that the agreement is generally satisfactory, though a significant disagreement exists between the values of $\sigma_{el}$ obtained in this experiment and those obtained by Wikner,[29] whose values are more than twice as large. Wikner obtained total cross sections by extrapolating his small-angle cross sections linearly to 0 deg. His method can yield high values of the cross section for heavy nuclei because of Rutherford scattering at small angles, but this would not explain the disagreement between the results for beryllium and carbon. Wikner's values of $\sigma_{el}$ indicate a much larger real potential than that predicted from the optical model.

Table VI. Pion-nucleus absorption and elastic cross sections.

| | This experiment $\pi^+$ at 2.85 Bev ($\bar{\sigma}$ = 29.0 mb*) | | Wikner $\pi^-$ at 4.2 Bev ($\bar{\sigma}$ = 29.0 mb) | |
|---|---|---|---|---|
| | $\sigma_a$ (mb) | $\sigma_{el}$ (mb) | $\sigma_a$ (mb) | $\sigma_{el}$ (mb) |
| Be | 192± 8.0 | 41.5± 3.5 | 177± 9.0 | 125± 18 |
| C | 213± 8.0 | 66.6± 7.0 | 219± 8.0 | 167± 22 |
| Al | $428^{+15}_{-12}$ | $160.^{+14}_{-10}$ | 407±10 | 356±41 |
| Cu | $790^{+41}_{26}$ | $445.^{+60}_{-23}$ | 725±25 | 895±93 |

Nucleon-nucleus absorption and elastic cross sections

| | This experiment 2.2-Bev protons ($\bar{\sigma}$ = 43 mb*) | | Atkinson (Ref. 20) 5.0-Bev neutrons ($\bar{\sigma}$ = 38.5 mb) | | Ashmore et al. (Ref. 30) 24.0-Bev protons ($\bar{\sigma}$ = 38.5 mb) |
|---|---|---|---|---|---|
| | $\sigma_a$ (mb) | $\sigma_{el}$ (mb) | $\sigma_a$ (mb) | $\sigma_{el}$ (mb) | $\sigma_a$ (mb) |
| Be | 236± 4.0 | 64.8± 2.4 | | | 180 |
| C | 260± 6.0 | 107 ± 6.0 | 235±16 | 84±26 | 210 |
| Al | 503±16 | 236 ±17 | 381±27 | 233±42 | 400 |
| Cu | 914±44 | 620 ±65 | 586±25 | 572±42 | 710 |

*$\bar{\sigma}$ is the average of the cross sections for free protons and neutrons. The values listed were estimated from the best available data.

## ACKNOWLEDGMENTS

I am happy to take this opportunity to express my sincere gratitude to the many people whose help made this experiment possible. I particularly wish to thank Professor Burton J. Moyer for his aid and guidance in all phases of the experiment and the members of the group under his direction for their generous assistance. I am also indebted to Professor Kenneth Watson for advice on the theoretical aspects of the experiment, and to Graham Campbell for his help in computer programming.

- - - - - - -

This work was done under the auspices of the U. S. Atomic Energy Commission.

# APPENDIX I

## Calculation of the Electron Contamination

### A. Calculation of the Gamma Spectrum at the Bevatron Target

The $\gamma$ spectrum was calculated by using theoretical estimates of the yield of $\pi^0$ mesons produced by 7-Bev protons.[9] These theoretical curves were scaled down to 6 Bev, the energy of the circulating proton beam in the Bevatron, by multiplying the pion momenta by 6/7. Since the electron contamination depends only on the yield of $\pi^0$ mesons relative to $\pi^+$ mesons, this approximate procedure is justifiable.

Each $\pi^0$ decays into two $\gamma$'s of equal energy in the rest system of the $\pi^0$. The yield of $\gamma$'s at each energy and takeoff angle can therefore be calculated exactly from the corresponding information for $\pi^0$'s. In order to simplify the calculation some approximations are useful.

The angle between the path of the parent $\pi^0$ and that of the resulting $\gamma$ is typically on the order of 2 deg for $\gamma$'s of energy $>1.4$ Bev. If we neglect this angle and consider the $\gamma$'s as coming off at the same angle as the parent $\pi^0$, the yield of $\gamma$'s of energy $E_\gamma$ at an angle $\lambda$ from the circulating proton beam is*

$$\sigma_\gamma (E_\gamma, \lambda) = \int \sigma_\pi (E, \lambda) \cdot P(E, E_\gamma)\, dE, \qquad (I\text{-}1)$$

where $\sigma_\gamma$ and $\sigma_\pi$ are the $\gamma$ and $\pi^0$ yields, respectively, and $P(E, E_\gamma)\, dE_\gamma$ is the fractional probability that a $\pi^0$ of energy $E$ will produce a $\gamma$ with a lab energy between $E_\gamma$ and $E_\gamma + dE_\gamma$. For $0 < E_\gamma < E$ (limits are approximate), $P(E, E_\gamma)$ is constant:[31]

$$P(E, E_\gamma) = 1/E. \qquad (I\text{-}2)$$

Equation (I-1) therefore becomes

---

*This procedure is equivalent to averaging $\sigma_\pi$ over an interval of approx 2 deg about $\lambda$.

$$\sigma_\gamma (E_\gamma, \lambda) = \int_{E_\gamma}^{E_{max}(\lambda)} \sigma_\pi (E, \lambda)\, d(\log E). \qquad (I\text{-}3)$$

The $\gamma$ spectrum thus calculated is given in Fig. 22.

B. Calculation of the Electron Yield

At high energies the angle between the path of the parent photon and the electrons formed in pair production is very small. Furthermore, the energy distribution of the electrons is fairly flat between $E = 0$ and $E = E_\gamma$.[31] By the reasoning leading to Eq. (I-3), we obtain

$$\sigma_e(E_e, \lambda) \cong \int_{E_e}^{E_{max}(\lambda)} \sigma_\gamma(E, \lambda)\, \mathcal{P}(E, \lambda)\, d(\log E), \qquad (I\text{-}4)$$

where $\mathcal{P}$ is the probability that a photon of energy $E$ at an angle $\lambda$ will produce an electron pair. At high energies, $\mathcal{P}(E, \lambda)$ is essentially independent of energy and can be taken out of the integral. In the energy range of interest, $\mathcal{P} \approx 0.75$ for a path length of one radiation length.[31] In general,

$$\mathcal{P}(E, \lambda) = 1 - \exp\left[-1.35\, \bar{L}(\lambda)/L_{rad}\right], \qquad (I\text{-}5)$$

where $\bar{L}(\lambda)/L_{rad}$ is the average path length of the $\gamma$'s in the target material in radiation lengths. The factor of 1.35 is necessary to make $\mathcal{P}(E, \lambda) = 0.75$ for $\bar{L}(\lambda)/L_{rad} = 1$.

C. Calculation of $\bar{L}(\lambda)$

Referring to Fig. 7, we see that the average (available) path length in the target material is

$$\bar{L}(\lambda) = \frac{\int dx \int N(y) \cdot L(x, y, \lambda)\, dy}{\int dx \int N(y)\, dy}, \qquad (I\text{-}6)$$

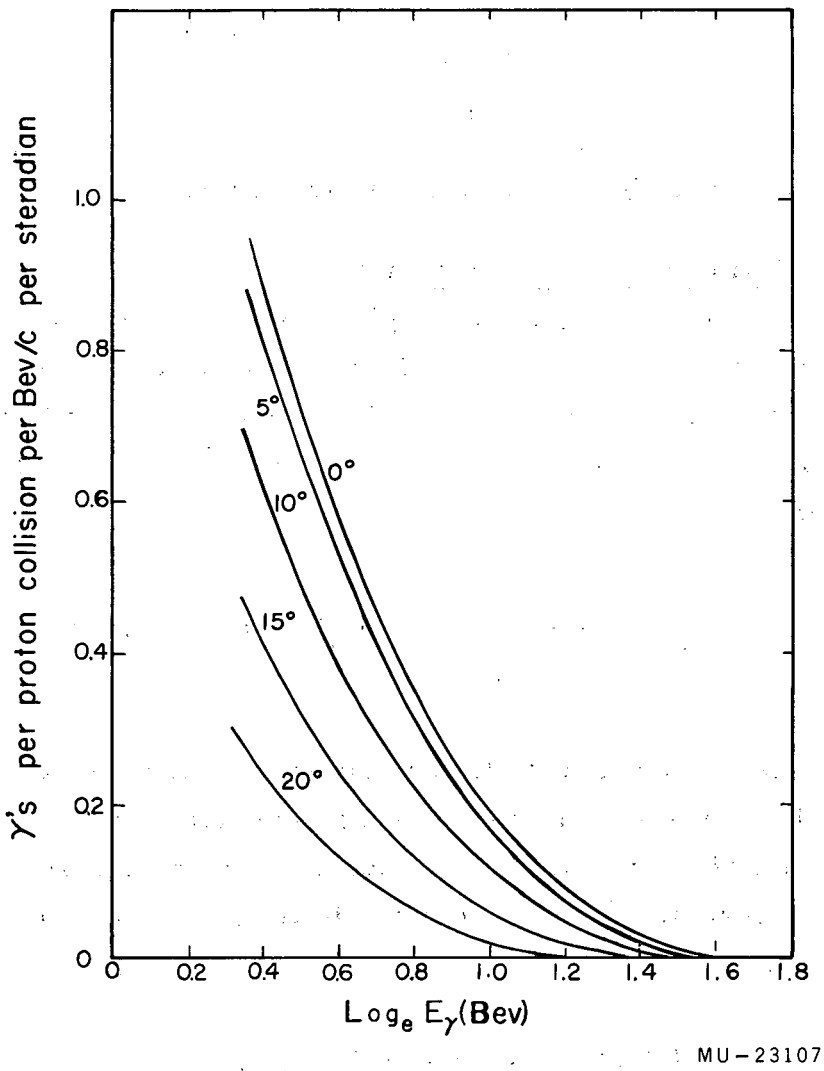


Fig. 22. The yield of γ's vs energy at the Bevatron target for various takeoff angles. To obtain absolute yields, the ordinate must be multiplied by approx 0.33.

where N(y) is the distribution in y of the proton flux striking the target. The slight dependence of N on x was neglected. N(y) was taken from curves given in Ref. 32.

D. Correction of the Calculated Contamination for Pion Decay

The electron contamination near the Bevatron target is $\sigma_e/(\sigma_e + \sigma_{\pi^+})$, where $\sigma_e$ is the electron yield given by Eq. (I-4) and $\sigma_{\pi^+}$ is the $\pi^+$ yield at the same beam momentum and angle.[9] The electron contamination near the end of the counter telescope is approximately 25% larger because of decay in flight of the pions.

## APPENDIX II

### Generalization of Eq. (21) to Include the Finite Angular Resolution of the Counter System

If the finite angular resolution of the counter system is taken into account, Eq. (21) must be replaced by

$$\sigma(\theta) = \int_0^{\pi} \frac{d\sigma_{el}(\theta')}{d\Omega'} \mathcal{R}(\theta, \theta')\, d\Omega' + \sigma_a - 2\pi\, \eta(1-\cos\theta), \qquad \text{(II-1)}$$

where $\mathcal{R}(\theta, \theta')$ is the probability that a particle scattered at an angle $\theta'$ will miss the transmission counter. For a system with perfect angular resolution, $\mathcal{R} = 0$ for $\theta' < \theta$ and $\mathcal{R} = 1$ for $\theta' > \theta$. In general, $\mathcal{R}(\theta, \theta')$ depends on the radius R of the transmission counter and the beam distribution at the transmission counter with the absorber out of the beam.

Let $R \equiv \theta L$ and $R' \equiv \theta' L$, where L is the distance between the absorber and the transmission counter. (We assume small angles, and in what follows we neglect the finite thickness of the absorbers, which was on the order of 1 inch.) Consider a beam particle which, if undeflected in a nuclear interaction, strikes the transmission counter at a distance a from its center. Let $P(a, R, R')$ be the probability that this particle will miss the transmission counter if scattered through an angle $\theta' = R'/L$. Then we have

$$\mathcal{R}(R, R') = \int P(a, R, R') \cdot B(a)\, a\, da \Big/ \int B(a)\, a\, da, \qquad \text{(II-2)}$$

where B(a) is the beam distribution given in Fig. 5.

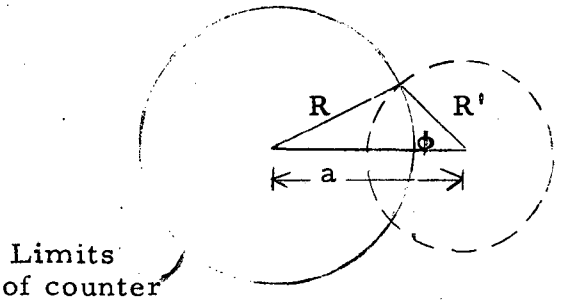


Fig. 23. Geometry for calculating P(a, R, R').

Referring to Fig. 23, we see that P(a, R, R') is the fraction of the circumference of the dotted circle with radius R' that is outside the solid circle (radius R). For R' < R,

$$1 - P(a, R, R') = \begin{cases} \phi/\pi & \text{for } R-R' < a < R+R', \\ 0 & \text{for } a \geqslant R+R', \\ 1 & \text{for } a \leqslant R-R', \end{cases}$$

and for R' > R,

$$1 - P(a, R, R') = \begin{cases} \phi/\pi & \text{for } R'-R < a < R'+R, \\ 0 & \text{for } a > R+R', \\ 0 & \text{for } a < R'-R, \end{cases} \qquad \text{(II-3)}$$

where $\phi = \cos^{-1}\left(\frac{a^2+R'^2-R^2}{2aR'}\right)$, $\qquad 0 \leqslant \phi \leqslant \pi.$

The function $\mathcal{K}(\theta, \theta')$ was calculated for each experimental point (each value of $\theta$), and the first term on right-hand side of Eq. (II-1) was evaluated by numerical integration with the $(d\sigma/d\Omega)_{el}$ calculated for each $U_0$ and $V_0$. The difference between $\sigma(\theta)$ calculated from the approximate Eq. (21) and Eq. (II-1) was approx 2% at most.

Multiple elastic scattering in the absorber has an effect similar to that of the finite angular resolution of the counter system. The first scattering(s) serves to "aim" the particle at some point on the transmission counter other than its center, thus making the final scattering ill-defined. The probability of multiple nuclear scattering was small with the absorber thicknesses chosen, and, in view of the small effect of the finite angular resolution, was neglected. This was verified experimentally by varying the thickness of the absorber. Halving the amount of beryllium had no significant effect on the cross sections at intermediate geometries (see Section IV.B).

## REFERENCES


1. A complete list of references on dispersion relations is available in an article by Dr. G. Chew in Ann. Rev. Nuclear Sci. 9, 29 (1959).
2. J. H. Atkinson and V. Perez-Mendez, Rev. Sci. Instr. 30, 865 (1959).
3. William A. Wenzel, Millimicrosecond Coincidence Circuit, UCRL-8000, Oct. 1957. The Lawrence Radiation Laboratory Counting Handbook, UCRL-3307 Rev., describes all the counting equipment used in this experiment.
4. D. F. Swift and V. Perez-Mendez, Rev. Sci. Instr. 30, 1004 (1959).
5. D. D. Newhart, V. Perez-Mendez, and W. L. Pope, Liquid Hydrogen Target, UCRL-8857, Aug. 1959.
6. Wooley, Scott, and Brickwedde, J. Research Natl. Bur. Standards 41, 379 (1948).
7. R. M. Sternheimer, Rev. Sci. Instr. 25, 1070 (1954).
8. W. Barkas and A. H. Rosenfeld, Data for Elementary-Particle Physics, UCRL-8030, March 1958.
9. D. Morgan, Some Theoretical Estimates of the Yield of Secondary Particles Produced by 7-Gev Protons, Atomic Energy Research Establishment (Harwell), Report R3242, February 1960.
10. Burrowes, Caldwell, Frisch, Hill, Ritson, and Schluter, Phys. Rev. Letters 2, 117 (1959).

11a. F. Chen, C. Leavitt, and A. Shapiro, Phys. Rev. 99, 857 (1955).

b. Von Dardel, Frisch, Mermod, Milburn, Piroué, Vivargent, Weber, and Winter, Phys. Rev. Letters 5, 333 (1960).

c. Brisson, Detoeuf, Falk-Vairant, von Rossum, and Valladas, Mesure de la Section Efficace Totale $\pi^+$-p et $\pi^-$-p de 400 Mev a 1.5 Gev, Submitted to Nuovo cimento.

d. Thomas J. Devlin (Lawrence Radiation Laboratory), private communication. Preliminary data appear in Phys. Rev. Letters 4, 242 (1960).

12. R. Lipperheide and D. S. Saxon, Phys. Rev. 120, 1458 (1960).
13. R. M. Frank, J. L. Gammel, and K. M. Watson, Phys. Rev. 101, 891 (1956).
14. W. B. Riesenfeld and K. M. Watson, Phys. Rev. 102, 1157 (1956).
15. James W. Cronin, Phys. Rev. 118, 824 (1960).
16. K. M. Watson and C. Zemach, Nuovo cimento 10, 452 (1958).
17. T. K. Fowler and K. M. Watson, Nuclear Phys. 13, 549 (1959).
18. W. M. Preston, Richard Wilson, and J. C. Street, Phys. Rev. 118, 579 (1960).
19. V. S. Barashenkov and Huang Nen-ning, J. Exptl. Theoret. Phys. (U.S.S.R.) 36, 832 (1959) [translation: Soviet Phys.-JETP 36 (9), 587 (1959)].
20. John H. Atkinson, 5-Bev Neutron Cross Sections in Hydrogen and Other Elements (Ph. D. Thesis), UCRL-8966, Nov. 1959.
21. Herman Feshbach, The Optical Model and Its Justification, Ann. Rev. Nuclear Sci. 8, 49 (1958).
22a. Robert Hofstadter, Rev. Modern Phys. 28, 214 (1956).
b. Robert Hofstadter, Ann. Rev. Nuclear Sci. 7, 231 (1957).
23. F. Bjorklund, I. Blandford, and S. Fernbach, Phys. Rev. 108, 795 (1957).
24. L. I. Schiff, Quantum Mechanics, (McGraw-Hill Publishing Co., N. Y., 1955), Ch. XII.
25. K. Gatha and R. Riddell, Jr., Phys. Rev. 86, 1035 (1952).
26. J. W. Cronin, R. Cool, and A. Abashian, Phys. Rev. 107, 1121 (1957).
27. I. Pomeranchuk, J. Exptl. Theoret. Phys. (U.S.S.R.) 34, 725 (1958) [translation: Soviet Phys.-JETP 34 (7), 499 (1958)].
28. S. D. Drell, Phys. Rev. Letters 5, 342 (1960).
29. Frederick Wikner, Nuclear Cross Sections for 4.2-Bev Negative Pions (Ph. D. Thesis), UCRL-3639, January 1957.
30. A. Ashmore, G. Cocconi, A. N. Diddens, and A. M. Wetherell, Phys. Rev. Letters 5, 576 (1960).

31. Bruno Rossi, High-Energy Particles (Prentice-Hall Inc., N. Y., 1952).

32. J. W. Burren, The Extraction System for Nimrod (Part I), Atomic Energy Research Establishment (Harwell) Report M521, November 1959.